

Superconducting Electronics for Breakthrough Starshot Communications

by

Andrew Sorenson

B.S. Electrical Science and Engineering and Physics  
Massachusetts Institute of Technology, 2021

Submitted to the Department of Electrical Engineering and Computer Science  
in Partial Fulfillment of the Requirements for the Degree of

Master of Engineering in Electrical Engineering and Computer Science

at the

MASSACHUSETTS INSTITUTE OF TECHNOLOGY

May 2022

©2022 Massachusetts Institute of Technology. All rights reserved.

Signature of Author: .....

Department of Electrical Engineering and Computer Science  
May 13, 2022

Certified by: .....

Karl K. Berggren  
Professor of Electrical Engineering and Computer Science  
Thesis Supervisor

Accepted by: .....

Katrina LaCurts  
Chair, Master of Engineering Thesis Committee



# Superconducting Electronics for Breakthrough Starshot Communications

by

Andrew Sorenson

Submitted to the Department of Electrical Engineering and Computer Science on May 13, 2022 in Partial Fulfillment of the Requirements for the Degree of Master of Engineering in Electrical Engineering and Computer Science

## ABSTRACT

Gram-scale sailcraft for the Breakthrough Starshot project are currently being designed to travel to Proxima Centauri, 4.24 light years away, and transmit back images and data [1]. In order to meet the size, weight, and power constraints of the mission, superconducting electronics should be considered for onboard processing and interfacing with the communications system. Previous research has shown that superconducting nanowire electronics consume over 100x less switching energy than 7 nm CMOS electronics [2]. In order to pursue application of superconducting electronics on Starshot probes, fundamental questions must be answered regarding the suitability of superconducting materials in the interstellar environment. To investigate this suitability, we performed numerical analysis of the effects of both radiation and temperature on superconducting electronics. We also designed, simulated, and tested superconducting nanowire devices tailored to Starshot operations. We found that with an edge-on sail transit configuration, equilibrium temperature of the sail may be below the critical temperature of common superconductors and that the anticipated error rate from radiation is  $1.23 \times 10^{-18} \mu\text{m}^{-2} \text{ns}^{-1}$ . We also present the design and simulation of a circuit modification that may drastically reduce the error rate in exposed superconducting nanowires. By finding that there are no immediate show-stoppers for using superconducting electronics onboard, we hope to inspire future investigations into the use of superconducting nanowire electronics for Starshot and other deep space missions.

Thesis Supervisor: Karl K. Berggren

Title: Professor of Electrical Engineering and Computer Science



## Acknowledgements

This work would not have been possible without the help and advice of my colleagues, friends, family, and mentors. In particular, I would like to thank the following people who have helped me over the last year:

My advisor Prof. Karl K. Berggren, for his constant mentorship and sharing of knowledge. I would like to thank Karl for allowing me to work on such an exciting project, and welcoming me into the group with open arms. He has been a great source of technical expertise and guidance in conducting meaningful research.

I would also like to thank Dr. Tony Zhou for mentoring me since day one. Tony, your help in my transition into the group allowed me to have a positive experience in academia, which I truly value. Thank you for spending time discussing ideas, teaching me fabrication methods, supporting my interests, and reinforcing good research practices.

In addition, I would like to thank Owen Medeiros and Marco Colangelo for sharing their expertise of the lab equipment and resources for device fabrication and testing. Thank you for spending time to teach me and discuss my ideas. Thank you also to Mackenzie LeVangie for her help in sputtering the superconducting films for these devices and maintaining our shared lab space. I am also very appreciative of the administrative support from Dorothy Fleischer and Rinske Wijtmans.

I would like to thank Adina Bechhofer and Emma Batson for their company in the office and technical discussions that fueled this research. I thank the rest of the superconducting team and QNN group for their discussions and collaboration throughout the year.

I thank the Breakthrough Foundation for funding the Breakthrough Starshot project and supporting this research. I also thank MIT for fostering an amazing academic and research environment, and being the source of so many of my cherished friendships and experiences.

I would like to thank my parents, Michele and Brian Sorenson, for their endless support and gentle guidance to keep me on track. Lastly, I'd like to thank my brother Christian for being a role model and stable influence in my life, but always challenging me to improve.

## List of Figures

1.1	Critical Temperature of Superconductors	16
2.1	Starshot Probe Mission Diagram	24
2.2	Van Allen Radiation Belts	25
2.3	Galactic Cosmic Ray Energy Spectra	27
2.4	Electronic and Nuclear Stopping Power	32
2.5	Stopping Power Graphs of Molybdenum	33
3.1	Starshot Radiation Simulation Diagram	38
3.2	Pseudocode for Total Radiation Dose Calculation	39
3.3	Comparison of Expected and Calculated Stopping Power	40
3.4	Starshot Transit Configurations	41
3.5	Possible Superconducting Material Geometries	42
3.6	Hotspot Formation in Superconducting Nanowires	46
3.7	Radiation Error in Superconducting nTron	48
3.8	Face-on Sailcraft Temperature	49
4.1	Superconducting OR Gate Schematic	54
4.2	Cascade of Two Superconducting Devices	55
4.3	General Superconducting Interconnect Model	56
4.4	SPICE Schematic for Interconnect Simulation	57
4.5	Radiation-Free AC Current Plot	58
4.6	AC Current Plot with Radiation Exposure	58
4.7	Radiation-Free DC Current Plot	59
4.8	DC Current Plot with Radiation Exposure	60
4.9	SPICE Schematic for Shunted Interconnect Simulation	61
4.10	AC Current with Radiation and Shunt	62
4.11	DC Current with Radiation and Shunt	63
5.1	Planar hTron with SNSPD Layout	65
5.2	Planar hTron Layout	66

5.3	SEM of phTron-SNSPD Device .....	67
5.4	PCB for Cryogenic Testing .....	68
5.5	PCB and Sample in Testing Apparatus .....	68
5.6	Cryogenic Testing Apparatus .....	69
5.7	I-V Plots for phTron A .....	71
5.8	I-V Plots for phTron B .....	71
5.9	Double Sweep of phTron A .....	73
5.10	Double Sweep of phTron B .....	73

# Contents

<b>1</b>	<b>Introduction</b>	<b>10</b>
1.1	Superconducting Electronics in Deep Space	11
1.1.1	Deep Space Applications	12
1.1.2	Challenges for Electronics	12
1.1.3	Suitability of Superconducting Electronics	14
1.2	Breakthrough Starshot Project	16
1.2.1	Propulsion	17
1.2.2	Lightsail Structure	17
1.2.3	Communications	18
1.3	Thesis Goal	20
1.2	Thesis Outline	20
<b>2</b>	<b>Radiation in Space</b>	<b>22</b>
2.1	Space Radiation Environment	22
2.1.1	Modes of Radiation in Space	22
2.1.2	Distinct Regions of Radiation	23
2.1.3	Trapped Radiation	24
2.1.4	Solar Particle Events	26
2.1.5	Galactic Cosmic Rays	26
2.1.6	Interstellar Gas and Dust	28
2.1.7	Radiation in the Proxima Centauri System	30
2.2	Quantifying Radiation	31
2.2.1	Classifying Radiation	31
2.2.2	Stopping Power of Ionizing Particles	34
<b>3</b>	<b>Effects of Radiation on Superconducting Electronics</b>	<b>37</b>
3.1	Starshot Radiation Model	37
3.1.1	Simulation Setup and Model	37
3.1.2	Simulation Results	39

3.2	Effects of Radiation on Superconductivity in Nanowires .....	45
3.2.1	Breaking Superconductivity .....	45
3.2.2	Impact on Electronics .....	47
3.3	Heating of Sailcraft .....	48
<b>4</b>	<b>Design of Radiation Hard Superconducting Electronics</b>	<b>52</b>
4.1	Motivation for Resilient Devices .....	52
4.2	Generalized Interconnect Model .....	55
4.3	Shunted Interconnect Design .....	60
<b>5</b>	<b>Fabrication and Testing of Superconducting Electronics</b>	<b>64</b>
5.1	Layout of Devices .....	64
5.2	Fabrication Methodology .....	66
5.3	Early Results .....	69
<b>6</b>	<b>Conclusions and Future Work</b>	<b>75</b>
6.1	Operability of Onboard Superconducting Electronics .....	75
6.2	Superconducting Electronics in Starshot Ground Station .....	76
6.3	Future Work .....	77

# 1 Introduction

In 2022, fifty years after the last person walked on the moon, humanity is signaling that it is once again ready to explore space. NASA's Artemis Plan intends to land humans on the moon again in 2024 and establish a protocol for deeper exploration towards Mars [3]. The Europa Clipper, a NASA mission to determine the suitability of life on Jupiter's icy moon Europa, is scheduled to launch in 2024 and begin surveying the potential oceans of Europa in 2030 [4]. In order to facilitate progress into deep space, beyond the moon, the Deep Space Optical Communications project was established to lay the framework for a high-speed optical communications highway that is 10-100x faster than current radio communications between Earth, Mars, and beyond [5].

These missions offer great opportunities to understand new science, but they also introduce a new generation of technological challenges in both the physical design of spacecraft that can operate in deep space, but also the electrical and sensing systems that will be onboard. New generations of deep space vehicles must tackle the problem of propulsion: how to traverse incredible distances within a reasonable time scale. Chemical propulsion has historically been the only practical mechanism for propelling spacecraft, but even with optimizations and advancements the speed limit for chemically-propelled vehicles is on the order of  $\sim 10$  km/s [6]. Within the solar system this yields travel times of about 6 months to Mars and 5 years to Jupiter. If the destination were another star system, the travel time would be tens of thousands of years. The problem of propulsion must be solved should humanity ever truly explore the stars. Thermal issues also pose a challenge to spacecraft. In the case of some systems, such as the James Webb Space Telescope's imagers, it is desirable for the temperature to remain extremely low (about 50 K) [7]. Yet for many others, such as spacecraft with traditional military grade electronics that have temperature ratings from  $-55^{\circ}\text{C}$  to  $125^{\circ}\text{C}$ , the temperature is constrained to a relatively small range [8]. In deep space, the question of thermal management will be more profound than when orbiting Earth because temperature swings resulting from direct sunlight may be even more severe. New spacecraft intended for deep space exploration must meet these challenges of physical design and thermal management.

Electrical systems onboard deep space craft also face new challenges not frequently encountered in traditional spacecraft. These challenges manifest not only in the capabilities of the electronics, with regard to processing power and communications, but also in the constraints

they face, such as operating temperature, available power, and environmental radiation. Communications with spacecraft can be difficult even in Earth orbit, where satellites generally face a bottleneck in transmitting data to and from the ground [9]. This limitation prevents bulk download of large data sets and transmission of precise navigational data. For spacecraft in deep space, the challenge of high speed communications will be more difficult, yet also more crucial to solve. Onboard processing capabilities must also be prioritized for new generations of deep space crafts. In order to accommodate new technologies, such as the Mars Ingenuity autonomous helicopter, spacecraft must be able to support rapid computations for navigation, sensing, vision processing, and control mechanics [10]. By enabling these functions, spacecraft in deep space will be able to operate autonomously in foreign environments, while recording and transmitting large quantities of scientific data.

These challenges fuel exploration of innovative technologies, with the possibility of huge breakthroughs that could change the way we approach deep space exploration. Two such technologies are lightsail-propelled spacecraft and superconducting sensors and elements for electronics. Neither of these ideas have been implemented at any scale in space, but both open the possibility for advances in propulsion and electronics of deep spacecraft. My thesis investigates the feasibility of operating superconducting electronics on spacecraft, particularly onboard a wafer-scale spacecraft propelled by a lightsail. The lightsail project, called Breakthrough Starshot, is discussed in detail in Section 1.2.

## **1.1 Superconducting Electronics in Deep Space**

Novel solutions must be considered to satisfy the unique electrical requirements of spacecraft operating in deep space. In particular, technologies should be explored that can leverage the environment of deep space to solve the challenges facing deep space electronics, which are examined in Section 1.1.2. This paper investigates the use of superconducting nanowire electronics in space. These electronics are an area of increasing research, with sensing, logic, and memory elements already demonstrated [11, 12, 13].

### **1.1.1 Deep Space Applications**

Many relevant applications are already in place for new deep space electronic technologies. The Deep Space Optical Communications project could greatly benefit from robust and efficient electronics onboard space-based relay stations [5]. These electronics would be responsible for interfacing with optical sensors, signal processing, driving optical transmitters, and performing operational electrical processes. Probes intended for exploration of the solar system could also benefit from suitable deep space electronics to perform signal analysis, onboard processing, and driving of transceivers. For example, the Europa Clipper probe intends to operate a Synthetic Aperture Radar (SAR) while orbiting Europa to perform detailed surface mapping and sounding of ice thickness [14, 15]. This dual frequency radar has a maximum data rate of 80 Mbps and records up to 24 Gb per flyby. Whether through onboard processing and compression, or high speed communications back to Earth, the spacecraft's electronics must be able to handle large data recordings. Missions even further into space, beyond our solar system, would benefit from electronics developed specifically for deep space operation. Discussed thoroughly in [16], an interstellar lightsail probe would benefit from electronics with advanced power and thermal management. The Breakthrough Starshot mission, discussed more in Section 1.2, is just one example of a deep space application for suitable advanced electronics.

### **1.1.2 Challenges for Electronics**

A multitude of challenges exist when designing and operating electronics on spacecraft, particularly in deep space. The most apparent challenges are communication limits back to Earth, total processing power, operating temperature, radiation exposure, and power requirements.

As discussed in the previous section, next generation deep space probes will record vast quantities of data. While onboard processing and compression may reduce the total amount of data to be transmitted back to Earth, there will still be a high data transfer requirement.

Traditional communication using radio frequencies imposes strict data transfer limitations, especially across vast distances [17]. Higher transfer rates can be achieved by using methods with a larger bandwidth, higher signal power, or lower noise level. In order to satisfy higher

transfer requirements, electronics on deep spacecraft may need to utilize optical communications, which yield a theoretical boost in data transfer rate of almost 50x [17].

For probes and spacecraft, particularly those performing complex computational functions such as SAR mapping or autonomous navigation, onboard electronics must be able to handle the intense computational load required during peak processing demand. This may not come as a challenge for electronics currently used on Earth, but enabling similar capacity in electronics rated for deep space operation may be difficult.

A spacecraft's temperature also poses challenges for operation of its electronics. Space agencies have optimized thermal management for satellites and space vehicles over the past 75 years to perform a delicate balancing act between heating from the sun and radiative cooling into space, all in order to keep a spacecraft's temperature within a defined range [18]. Other systems, particularly Radioisotope Thermoelectric Generators (RTG), also exist to provide heating to spacecraft [19]. RTG's are common for spacecraft in deep space because the heating power from the sun diminishes quadratically with respect to distance. In order to operate electronics, which are generally rated from  $-55^{\circ}\text{C}$  to  $125^{\circ}\text{C}$ , a thermal generator is needed to balance the heat dissipated into space from the spacecraft's outward thermal radiation. By changing the operating temperature of electronics, one can completely change the operating temperature of the entire spacecraft. The challenge of thermal management is discussed more thoroughly in Chapter 5.

Radiation in space also presents challenges to electronics. Without the protection of Earth's magnetic field, objects in space are subject to radiation ejected from the sun, radiation flying through the cosmos, and even radiation trapped in orbit within Earth's magnetosphere [20]. As spacecraft operate, their electronics are exposed to varying levels of radiation, depending on the amount of shielding present. Radiation that interacts with electronics can cause various negative effects, generally classified as either a total dose effect or a transient effect [21]. Total dose effects refer to permanent material effects that could impact normal electronic operations, such as lattice vacancies or interstitial atoms [21]. Transient effects are usually called Single Event Effects (SEE), and refer to instantaneous effects of radiation absorption, such as a bit flip in a memory element. SEEs can potentially be disastrous for spacecraft, especially when a single bit error inside a processing unit could have a cascading effect on logic. One notorious example of a SEE catastrophe is the failure of the Russian Phobos-Grunt mission to retrieve Martian solar samples [22]. After the spacecraft failed just days after launch, an investigation

commenced and concluded that electronic components onboard were unsuitable for the space radiation environment and determined with high likelihood that the cause was a bit error in the electronics, caused by cosmic radiation [22]. Radiation poses a challenge for all electronics in space.

Power limitations are an extreme influence on the design of electronics for spacecraft, particularly in deep space. Current spacecraft generate power either through the use of photovoltaics or radioisotope thermoelectric harvesters [23]. Depending on a craft's power budget and distance to the sun, solar arrays may be able to yield all the power required for operation. With modern photovoltaic technology, a power generation efficiency of up to 30% can be achieved [23]. In situations where spacecraft operate far from the sun, such as in the Voyager missions, thermoelectric generators coupled with a radioisotope heater are needed to generate power for onboard equipment [24]. Power requirements vary across missions, but design optimization can result in electronics and equipment with extremely low power requirements, making the challenge of power generation more simple to solve. Within electrical processing components, the total power needed can be expressed as  $P_{total} = P_{DC} + P_{AC}$  [25]. Total power required is a sum of the power needed for DC biasing and AC switching events. In order to minimize power requirements for electronics, engineers can reduce the number of processing components (transistors) needed or reduce  $P_{DC}$  or  $P_{AC}$ . For future deep spacecraft, engineers must continue to ensure that power generation capabilities exceed electrical power requirements.

### 1.1.3 Suitability of Superconducting Electronics

Superconducting electronics should be considered for use in deep space due to their unique attributes of low power consumption, low operating temperature, and robustness.

In terms of AC power consumption, superconducting logic elements may require over 100x less switching power than conventional 7 nm CMOS devices [2]. This assumes a bias current of 10  $\mu A$ , which is feasible for superconducting devices. While research still needs to be conducted to determine the lower limit for static power dissipation possible with these devices, it seems very possible to employ superconducting logic elements for ultra-low power processing.

The low operating temperature of superconducting devices also presents suitability for operation in deep space. With low electronic operating temperatures, spacecraft in deep space

may be able to lower their overall temperature, resulting in a lower power requirement since heaters may not be required. In addition to power savings by operating electronics at a lower temperature, superconducting electronics are also ideal for interfacing with cold sensors such as telescopes. A current example of this is the James Webb Space Telescope. Although its mirrors are cooled to 50 K, onboard electronics remain thermally isolated and operate at a higher temperature. Future space telescopes with cold sensors could avoid needing onboard thermal isolation for electronics by using superconducting electronics. With superconducting electronics, the entire spacecraft could be cold. The upper temperature limit of any superconducting device is the critical temperature ( $T_C$ ) of the material, beyond which it will no longer be superconducting. As seen in Figure 1, different materials have different critical temperatures. While most of the devices in our group are fabricated with NbN, which has a bulk  $T_C$  of around 15 K, other materials may be used for superconducting devices that permit higher temperature operation. However, many of these materials with higher critical temperatures present significant challenges in fabrication and cannot currently be patterned into reliable devices. They may also have poor resistance to radiation effects. The ability to dramatically reduce the operating temperature of spacecraft electronics with the use of superconductors presents many opportunities for development.

The robustness of superconducting devices could also make them optimal for operation in space. While this factor isn't strongly investigated in my thesis, the single-layer fabrication of superconducting devices may make them a strong candidate for electronics in deep space where temperature swings and radiation exposure present challenges. The issue of radiation is common in space and preliminary data indicates that NbN thin-films may have minimal damage from high radiation doses [26]. Measurements with a total neutron fluence of  $10^{23} \text{ m}^{-2}$  show only a 5.7% reduction in critical temperature and no measurable change in critical current density [26]. Chapters 2 and 3 examine radiation in more detail and specifically assess transient errors from radiation. While more investigation is required, superconducting devices may be suitable for space because of intrinsic robustness.

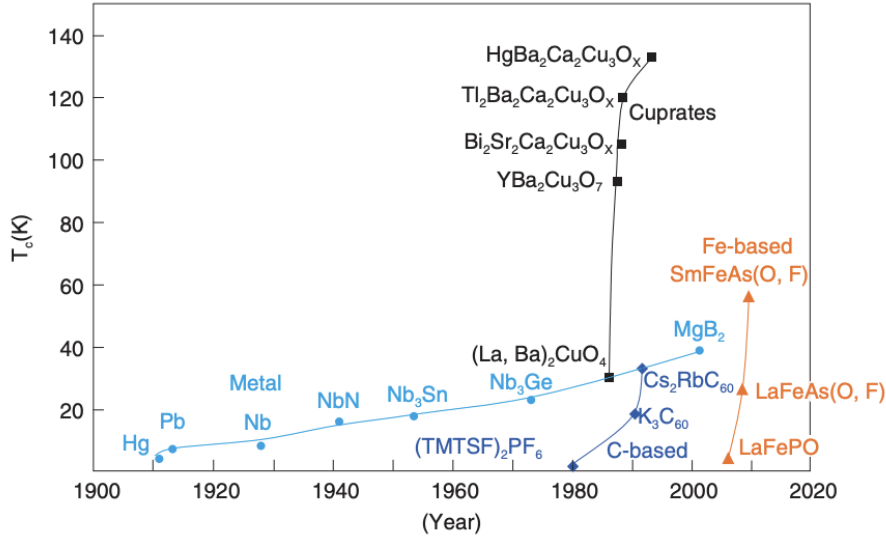


**Figure 1.1:** The critical temperature of various superconducting materials along with the year of their discovery. Figure reproduced from NTT Technical Review [27].

Unique physical and electronic characteristics of superconducting devices enable low temperature operation and ultra-low power consumption for electronics. These traits, in addition to possible robustness in the space environment, make superconducting electronics a candidate for deep space applications.

## 1.2 Breakthrough Starshot Project

Research for this thesis was funded by the Breakthrough Starshot project, an initiative to send a probe to the Proxima Centauri star system with the intention of transmitting back images and scientific data [1]. Although Proxima Centauri is the closest star to our Sun, it is still at a distance of 4.22 light years [1]. The project is strongly driven by the search for life beyond Earth. In 2016, scientists detected a small exoplanet orbiting Proxima Centauri within the habitable zone, a region where the liquid water may be supported on the surface of the planet [28]. The exoplanet was named “Proxima b.” It may be the nearest object in space that could support life as we know it. The technical vision for Breakthrough Starshot is to investigate this exoplanet, and the entire Proxima Centauri star system, using an ultra-light probe that is propelled by photons [1]. Multiple complex systems must be developed in order for this concept to succeed. Many magnitudes of improvement across domains such as laser arrays, nanostructures, low power

electronics, and lightweight optical communication systems must occur before the first Starshot probe can launch.

### **1.2.1 Propulsion**

The first question that has to be answered in order to conduct an exploratory mission to another star system is how to get there. Current missions in space primarily rely on chemical propulsion. A good example is the Voyager I probe, the farthest man-made object in space. Even at a speed of 17 km/s, Voyager I took 37 years to exit our solar system [16]. At that rate, it would take just shy of 75,000 years for a similarly propelled craft to reach the Proxima Centauri system. It's a risky bet that someone will be at mission control to receive data in 75 millenia. A better method of propulsion is needed.

In order to retrieve meaningful scientific data and images from Proxima Centauri within a generation, a lightweight laser-driven sail has been proposed as the propulsion mechanism. A large array of high powered lasers, with roughly 1 km<sup>2</sup> area, will accelerate the large, thin lightsail [16]. Although there are many uncertainties in the technologies required, the project request for proposals document indicated that a circular sail of diameter 4.1 m and thickness of 100 nm will be used. A 1 gram payload will be permitted, to include onboard processors, sensors, and communications equipment. Preliminary estimates suggest that a 100 GW laser array will be required to accelerate the probe to  $0.2c$  [29]. This array must also be able to track the sail as it is propelled. It will be a challenge to create such a large array with fine focusing and tracking capabilities.

### **1.2.2 Lightsail Structure**

The structure of the sail will be designed almost at the atomic level in order to ensure proper optical and tensile properties. In order to minimize heating of the probe during launch and maximize momentum transfer from the photons of the drive beam, the sail must have incredibly high reflectance and low absorptance. The wavelength of the drive laser has been proposed to range from 1000-1300 nm in order to avoid absorption in the atmosphere [16]. Therefore, the lightsail must be designed to have near unity reflectance in this range and beyond, to account for

redshifting of the laser as the sail accelerates. A thorough review of the optical challenges and structural requirements posed by Starshot is presented in [30].

The sail needs to survive the acceleration phase and the force imparted by the drive laser. In addition to just surviving, the sail must ride the laser properly in order to exit with a stable trajectory along the intended route. Though not discussed in this paper, methods of controlling reflectance profiles with metasurfaces are being actively pursued in the context of Breakthrough Starshot [31]. These profiles could provide significant stabilization forces. Once the lightsail is accelerated, it still faces possible damage in the interstellar medium from cosmic dust. At  $0.2c$ , collisions with stationary dust may result in high energy damage tracks in the sail material. As discussed in [16], rough calculations of damage from dust indicate that 10% of a  $10\text{ m}^2$  material will sustain damage along a journey to Proxima Centauri. This damage consists of vaporization from the high energy collisions with dust particles. Methods of mitigating and minimizing this damage include rotating the sail to be edge-on during flight and shielding the front edge with a heavier, protective layer [16]. This will be discussed more thoroughly in Chapter 3.

The challenges for the lightsail structure can be summarized as high reflectance and low absorptance in drive laser window; high thermal emissivity; robustness against collisions with interstellar dust; and ultra-low density. The fabrication approach for the lightsail will influence how superconducting materials can be incorporated into the structure and impact equilibrium sail temperature during transit.

### **1.2.2 Communications**

After acceleration, communication back to Earth becomes the most pressing task. While communications from Earth to the spacecraft may not even be implemented, downlink from the spacecraft back to Earth will be crucial for “signs of life,” indicating the spacecraft is still functioning, as well as the transmission of data from the Proxima Centauri system. Challenges to enabling this downlink are prevalent, and exist both in the Earth-based receiver array and the onboard transmitter.

The receiver station on Earth will consist of a very large array of optical detectors and be responsible for collecting the optical signals transmitted from the probes. After traveling for over 4 light years, a huge challenge on the ground will be to collect the signal and reconstruct the data

that is encoded. In various papers, Phil Lubin, Ian Morrison, and Dave Messerschmitt have discussed the challenges in ground reception and proposed optimal methods of communicating across interstellar distances, as in the Breakthrough Starshot project [32, 33]. Their work suggests that the ground receiver will likely consist of single photon detectors and time-tagging equipment to enable Pulse Position Modulation (PPM) communication. PPM relies only on the direct detection and time-tagging of photons, where information is encoded in the temporal spacing of photon bursts [33]. In theory, this could support the communication of large amounts of data, but the signal loss across the vast distance between the probe and the Earth makes it difficult to send much data with Starshot's constraints. In fact, a gigantic array of detectors will be needed on Earth to collect optical signals from the probe. The effective area of the array must be around 1 km<sup>2</sup> [33]. In addition to its large area and single photon detection equipment, the ground receiver must also have adequate band-pass filtering to reduce background noise. This is difficult because although we may know the transmission frequency on the probe, a Doppler shift will occur, lengthening the wavelength as received on Earth. If the probe were to slow down dramatically or experience some other form of unknown velocity change, the Doppler shift may be both significant and unknown. A solution to this is to receive telemetry data from the probe at short time intervals, to more continuously track the Doppler shift. Assuming a large array is used with optimal filtering and detection-tagging equipment, the ground station will then need to conduct post processing to recover the timing of the encoded signal and extra relevant information such as images of Proxima b. The ground station has critical importance in the downlink.

The transmitter on the probe must produce and point optical signals back to Earth. Onboard electronics must also capture images and data of the Proxima Centauri system during their 2 hour flythrough of the solar system. After the flythrough, the remainder of the probe's life is dedicated to transmitting back captured data. As specified in the project's request for proposals document, every probe should transmit back at least 100 KB of data directly to Earth. While a concept has been considered to create a daisy-chain of probes, with data being transmitted across the shorter distance between spacecraft, the Breakthrough committee currently requires that each probe prioritize direct transmission back to Earth. In order to perform transmission, the probe must have the power to drive the laser, the ability to point and focus the beam (accounting for planetary movement over the course of 4 light years), and onboard electronics to compress and

encode data. The critical challenge for the onboard components will be incorporating all of these systems on a thin lightsail.

The key challenges to enabling an optical downlink for Starshot probes are onboard power limitations, design of sufficient onboard optical sources, filtering of optical signals in the ground receiver, sensitive single photon detectors with ultra-low dark count in the ground station, and cost and complexity of ground array construction.

### **1.3 Thesis Goal**

The goal of my thesis is to explore the suitability of superconducting nanowire electronics in the context of the Breakthrough Starshot project. This includes examining the operation of superconducting devices in the radiation environment of space and predicting error rates and methods of error mitigation. It also includes design and fabrication of structures and devices with potential applications for Starshot electronics. Using planned parameters of the Starshot project, I intend to make a fair assessment of the propriety of superconductors for onboard electronics.

### **1.4 Thesis Outline**

Below you will find a summary of each subsequent chapter and a description of what you can expect to find in each.

In Chapter 2, Radiation in Space, I conduct a literature review of the general radiation environments in space. I emphasize the type and quantity of radiation in regions through which a Starshot probe will pass. I also discuss methods of quantifying radiation effects, such as electronic and nuclear stopping power.

In Chapter 3, Effects of Radiation on Superconducting Electronics, I discuss a simulation of the total and transient radiation that a Starshot probe will face during its mission. I also discuss the operational effects that radiation will have on superconducting devices as well as on the lightsail itself.

In Chapter 4, Design and Testing of Radiation Hard Superconducting Electronics, I will address the motivation and need for designing radiation hard superconducting electronics for Starshot. I also introduce a device design that can help to mitigate radiation errors in

superconducting electronics. I discuss simulations and test results of a fabricated device that employs my proposed radiation hardening mechanism.

In Chapter 5, *The Future of Superconducting Devices on Starshot Probes*, I discuss critical considerations for using superconducting nanowire electronics in Starshot spacecraft. These considerations include temperature, power, and sailcraft configurations.

In Chapter 6, *Discussion and Conclusion*, I highlight the findings of my research and discuss implications for the future of superconducting electronics for Starshot. I discuss future areas of research that will benefit from investigation, and conclude by making a case for superconducting nanowire electronics in space.

## **2 Radiation in Space**

Radiation is a hazard for both organisms and materials in space. Despite this, electronics onboard spacecraft must continue to function normally even when exposed to radiation. Therefore, the effects of radiation on a mission's electronics must be well understood prior to launch. In order to use superconducting electronics on spacecraft, particularly in deep space, we must understand both the effects of radiation and how to reduce errors to be within an acceptable threshold. The existing literature covering the effects of radiation on superconducting electronics, and superconductors in general, is thin; especially when compared to that of conventional electronics, since semiconductor-based electronics have been used in space and high radiation environments for decades. The goal of this chapter is to present a literature review of space radiation across various environments and to discuss methods of quantifying the interaction of space particle radiation with superconducting materials. Although we focused on radiation that a Breakthrough Starshot probe will experience along its spaceflight, much of this review will apply to any deep space mission.

### **2.1 Space Radiation Environment**

Radiation environments within space are phenomenally diverse; they can be local and concentrated, or they can be uniform across large volumes and hardly measurable. The future Breakthrough Starshot probes will face challenges navigating through both of these environments. In order to understand the implications of travel through these areas of radiation, I will first review literature in the field that describes the composition, intensity, and location of various radiation environments. After establishing the radiation environments through which the probe will travel, I will shift to discussing the damage and specific effects this radiation will cause to onboard superconducting nanowire devices.

#### **2.1.1 Modes of Radiation in Space**

Radiation in space comes in the form of both electromagnetic (EM) waves and atomic or subatomic particles. EM signals across the entire spectrum can be found in space and are often

used to learn more about the nature of the universe, by correlating particular events to a specific range of EM emission [34]. Atomic and subatomic particles, which have a rest mass (unlike EM waves), are also found throughout the universe.

This investigation into the effects of radiation on superconducting nanowire-based electronics for Starshot focused on particle radiation. We chose to do so for two reasons. First, more tangible damage can result from interactions with heavy particles versus electromagnetic waves found in interstellar space. Second, the vast majority of the probe's lifespan will take place in an environment with much more particle radiation than EM radiation [35].

### **2.1.2 Distinct Regions of Radiation**

The diversity of radiation environments in space makes it impossible to model the radiation Starshot will face as a constant factor. Rather, it is best to distinguish between different regions of radiation that the probe will face as it traverses the distance to its destination, the Proxima Centauri star system. These distinct regions of radiation align with spatial boundaries along the probe's journey, which are shown graphically in Figure 2.1. The probe begins in the vicinity of Earth, where it is exposed to radiation trapped by Earth's magnetic field. Upon departure from Earth but while within the heliosphere, the boundary between our solar system and interstellar space, the probe is then primarily exposed to particles emitted from the sun. Once outside the heliosphere, the probe is fully exposed to the particle radiation of interstellar space, known as Galactic Cosmic Radiation or Galactic Cosmic Rays (GCR). I must note that GCRs also penetrate the heliosphere, but their effect can be overshadowed by solar radiation, especially during periods of high solar activity.

A discussion of the findings of the literature review of particle radiation in these regions follows in the subsequent sections. This review did not investigate the underlying physics responsible for establishing these radiation zones. Rather, the emphasis was to gather information to help build a model to simulate quantitative effects of radiation on superconducting electronics.

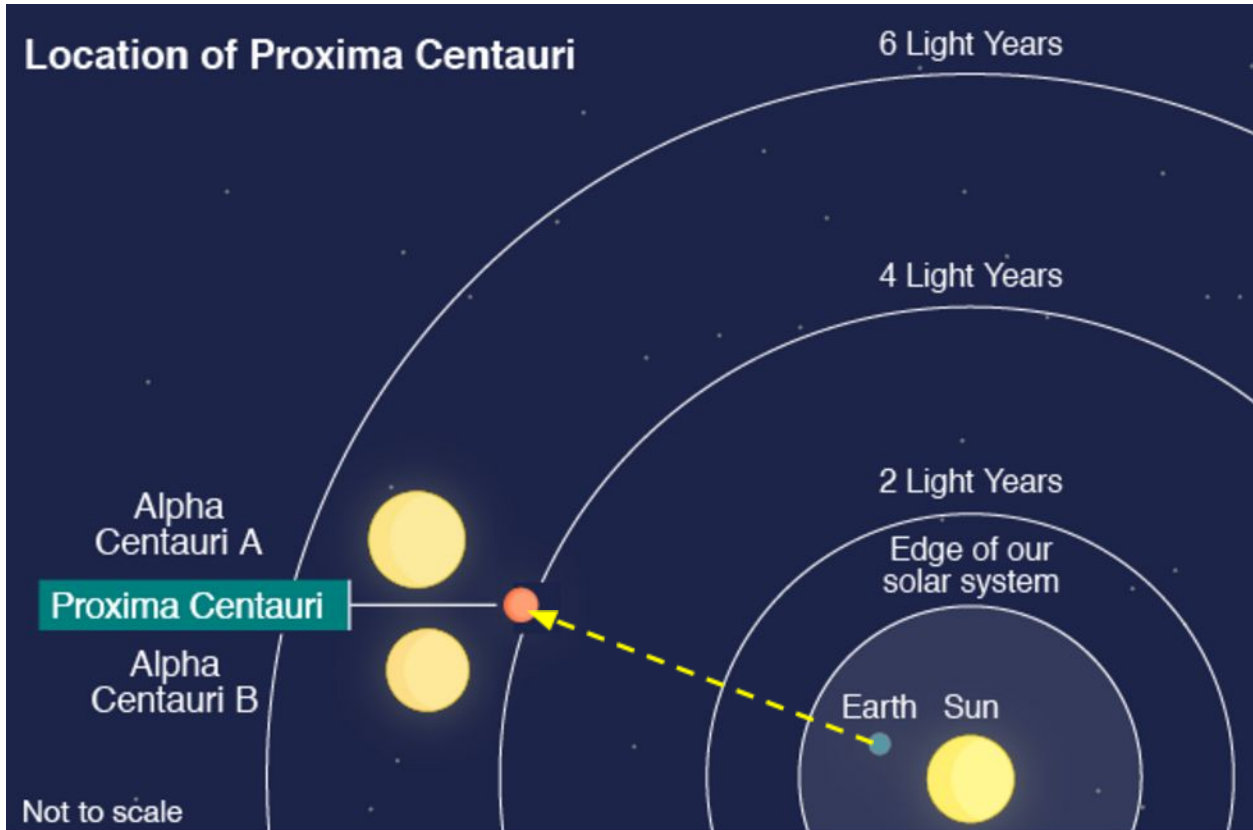


**Figure 2.1:** A graphic of the journey a Starshot probe will undertake, shown in dashed yellow. The probe will begin near Earth, where it is accelerated using a high powered laser array. Once at cruising speed, one fifth the speed of light, the probe will travel for over 20 years until it arrives in the Proxima Centauri star system. Once at its destination, the probe will capture data and transmit it back to Earth. Figure adapted from BBC News [36].

### 2.1.3 Trapped Radiation

The first region of the probe's journey will be the orbital environment around Earth. The probe will be deployed to this region via a rocket from Earth and will remain in orbit long enough for status testing prior to laser acceleration. While it is unknown exactly how long or at what altitude the probe will orbit, it may likely be placed into a geostationary orbit at an altitude of 35,785 km. By doing this, the probe will remain stationary as viewed by an observer on the ground. This will allow the ground-based laser array to accelerate the probe without having to make major aiming adjustments as the probe orbits.

Near Earth, the magnetic field generated by the planet's core can shield against certain types and energies of particle radiation, but it also produces regions with intense particle

radiation by trapping and accelerating particles [37]. These regions of intense radiation around Earth are called the Van Allen belts, and are depicted graphically in Figure 2.2.

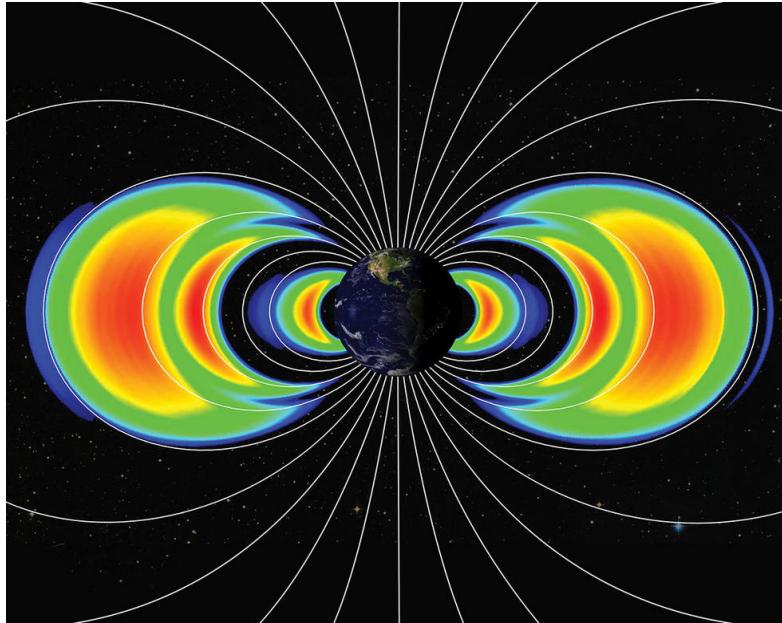


**Figure 2.2:** The Van Allen belts surrounding Earth. White lines are used to visualize the magnetic field surrounding Earth and a heat map is used to convey the relative amount of particle radiation, with red corresponding to areas with the highest radiation. Figure reproduced from NASA's Goddard Space Flight Center/Johns Hopkins University, Applied Physics Laboratory.

The belts primarily trap protons and electrons. Additionally, the interaction of GCRs with trapped particles can create free neutrons [38]. While these energetic particles pose a serious risk to objects and humans that travel through the radiation belts, we will ignore their effects for the purpose of this study. It is appropriate to do so because of the short duration in which the probe will be in the areas of high radiation and because the probe likely will still be shielded by its launch capsule until it reaches the target orbital altitude. This shielding will be appropriate to prevent significant damage from trapped radiation.

Once the probe has been placed into orbit, it will no longer have any other shielding and will be subject to the full radiation of the space environment. At geostationary orbit altitude, the probe is far enough away from the radiation belts to not receive any significant trapped radiation. However, this also means that Earth's magnetic field is weak, so there will be essentially no magnetic shielding from GCRs [20]. Once the probe is in orbit it will be subject to an

omnidirectional GCR flux for the duration of its lifespan. The composition and intensity of GCR radiation is specified in Section 2.1.5.

#### **2.1.4 Solar Particle Events**

Solar Particle Events (SPEs) encompass unusually large ejections of mass and energy from the sun, often in the form of a solar flare. These events cause large amounts of highly energetic particles to travel outwards from the sun. Studies indicate that these ejections are primarily composed of protons, but contain 5-10% alpha particles (helium nuclei). SPE likelihood depends on the current phase of the solar cycle, which has a period of roughly 11 years [20]. These events are particularly damaging for electronics in space not only because of the influx of high energy protons, but also because of the complex interaction they have with Earth's magnetic field and trapped radiation.

This radiation study did not strongly consider solar protons during analysis because a launch window can be chosen to greatly reduce the risk of a SPE occurring while the probe is in orbit around Earth. Once launched and accelerated to its cruising speed of  $0.2c$ , the probe will be outside the reach of solar ejections within days.

#### **2.1.5 Galactic Cosmic Rays**

In literature, Galactic Cosmic Rays are described as high-energy particles traveling through the cosmic medium. These particles stem from a variety of events such as normal emissions from stars as well as dramatic cosmic events such as pulsars and star-collapses [39]. They consist of subatomic particles and ionized atoms from across the periodic table. Due to dramatic and high-energy interactions between these particles and any matter they encounter, GCR atomic nuclei are fully ionized [39].

Observations of GCRs using balloons above Earth and space-based detectors has resulted in the GCR energy spectra presented in Figure 2.3.

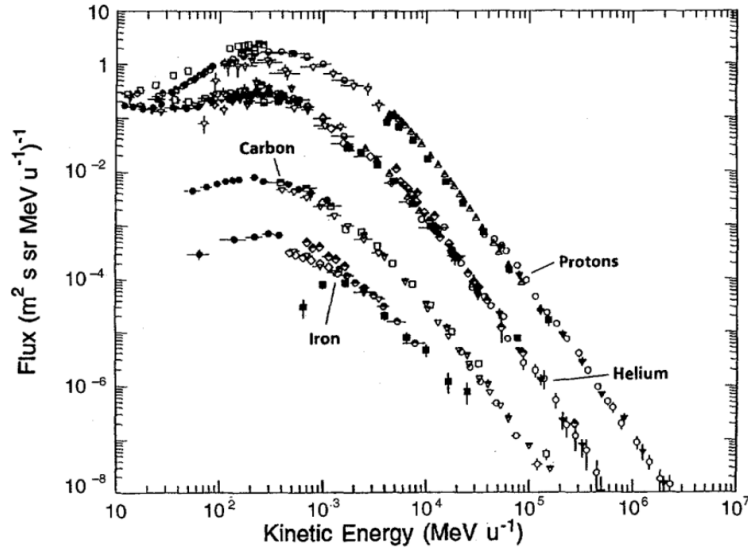


**Figure 2.3:** The energy spectra of dominant Galactic Cosmic Ray particles, measured near Earth. These spectra follow the trend that heavier particles have a lower flux than lighter particles. Figure reproduced from The Annual Review of Nuclear and Particle Science [39].

The information presented in Figure 2.3 is essential for quantifying the effects of GCRs on superconducting nanowire devices for Breakthrough Starshot or any other deep space application of superconducting nanowire electronics. From the figure we can extract the flux and corresponding energy of various GCR particles across their entire energy spectrum. For this initial investigation, we created a flux-energy “bucket” for each of the four dominant GCR particles (protons, He, C, Fe) around the region of the particle’s highest flux. These buckets are displayed in Table 2.1. The buckets were then used in a numerical simulation that calculated total energy absorbed by GCRs as well as electronic errors from GCR exposure. This simulation is presented in Chapter 3. For this simulation, we assumed full exposure to the entire GCR energy and composition spectrum beginning at the moment the Starshot probe leaves Earth’s magnetosphere upon laser acceleration.

**Table 2.1:** Flux-energy buckets extracted for each particle present in Figure 2.3. These buckets are used to simulate the effects of GCRs on superconducting electronics for Starshot.

<u>Particle</u>	<u>AMU [u]</u>	<u>Kinetic Energy [<math>\frac{MeV}{u}</math>]</u>	<u>Flux [<math>\frac{\#}{m^2 s}</math>]</u>
Proton	1	$2.7 \times 10^2$	$1.05 \times 10^3$
He <sup>2+</sup>	4	$2.7 \times 10^2$	$1.7 \times 10^2$
C <sup>6+</sup>	12	$4.0 \times 10^2$	4.6
Fe <sup>26+</sup>	52	$6.8 \times 10^2$	0.3

### 2.1.6 Interstellar Gas and Dust

Also clumped into the category of interstellar radiation is the gas and dust that occupies interstellar space. These exist in addition to the GCRs that permeate space. The interstellar medium is about 99% gas and 1% dust by mass, with over 90% of the gas consisting of hydrogen [16, 40]. Effects of dust grain damage are beyond the scope of this study, but have been discussed in [16], with the conclusion that the effects can be significantly minimized by reducing the cross section of the sail. I found that the stationary gas in interstellar space may likely be the biggest concern for on-board superconducting electronics. Although the gas is stationary, the high velocity of the spacecraft will result in energetic interactions with the gas it impacts. This hydrogen density is expected to be between  $0.07 - 0.24 \frac{H}{cm^3}$  [35, 41]. For our numerical simulation we use a gas density of  $0.3 \frac{H}{cm^3}$  in order to be conservative. This approximation is a density of neutral hydrogen atoms, but for the numerical simulation we treat this as a density of positive hydrogen ions because the energy of gas collisions is much larger than the binding energy of neutral hydrogen's electron. Therefore, we expect the hydrogen to be ionized for almost the entirety of its trajectory within the spacecraft.

We can create another particle bucket for interstellar gas by knowing its approximate density of  $0.3 \frac{H^+}{cm^3}$  and assuming a spacecraft velocity of  $0.2c$ . This velocity can be expressed in

different units as  $6.0 \times 10^9 \frac{cm}{s}$ . Multiplying this velocity by the density of  $0.3 \frac{H^+}{cm^3}$  results in an anticipated gas flux of  $1.8 \times 10^{13} \frac{H^+}{m^2 s}$ . In the rest frame of the spacecraft, the gas appears as a unidirectional stream of hydrogen nuclei impacting the spacecraft along the direction of its velocity vector's reciprocal, with a speed of  $0.2c$ . In order to complete the gas particle bucket for use in simulation, we calculated the kinetic energy (KE) of the gas particles in the rest frame of the spacecraft. We used Equation (2.1):

$$KE_{rel} = (\gamma - 1)mc^2, \quad (2.1)$$

the relativistic kinetic energy equation [42]. This expression of kinetic energy contains  $\gamma$ , the relativistic correction term, which is negligible for speeds  $v \ll c$ . Equation (2.2) presents the calculation of  $\gamma$ :

$$\gamma = \frac{1}{\sqrt{1 - \frac{v^2}{c^2}}}, \quad (2.2)$$

which is a function of  $v$ , the velocity of an object within an arbitrary rest frame [42]. For  $v = 0.2c$ ,  $\gamma = 1.0206$ , so the relativistic correction is only about 2%. As  $\gamma$  and  $v$  increase, calculation of kinetic energy using the relativistic formula in Eq. (2.2) becomes more important.

Using Eq. (2.1), we found the KE of the gas particles impacting the spacecraft will be  $19 \frac{MeV}{u}$ . This kinetic energy completes the new particle bucket for interstellar gas that will be used in simulation. This bucket is presented in Table 2.2.

**Table 2.2:** Flux-energy bucket for gas present in the interstellar medium. This bucket is valid only for gas impacting a spacecraft traveling at  $0.2c$ .

<u>Particle</u>	<u>AMU</u> [ $u$ ]	<u>Kinetic Energy</u> [ $\frac{MeV}{u}$ ]	<u>Flux</u> [ $\frac{\#}{m^2 s}$ ]
H <sup>+</sup>	2	$1.9 \times 10$	$1.8 \times 10^{13}$

**Table 2.3:** Flux-energy buckets for both GCRs and interstellar gas. These buckets are used to simulate the effects of GCRs on superconducting electronics for Starshot.

<u>Particle</u>	<u>AMU</u> [ $u$ ]	<u>Kinetic Energy</u> [ $\frac{MeV}{u}$ ]	<u>Flux</u> [ $\frac{\#}{m^2 s}$ ]
Proton	1	$2.7 \times 10^2$	$1.05 \times 10^3$
H <sup>+</sup>	2	$1.9 \times 10$	$1.8 \times 10^{13}$
He <sup>2+</sup>	4	$2.7 \times 10^2$	$1.7 \times 10^2$
C <sup>6+</sup>	12	$4.0 \times 10^2$	4.6
Fe <sup>26+</sup>	52	$6.8 \times 10^2$	0.3

Table 3 is the complete collection of particle buckets that are used to simulate effects of radiation on a Starshot spacecraft, as described in Chapter 3.

### 2.1.7 Radiation in the Proxima Centauri System

Once the probe arrives at the Proxima Centauri star system, there will be a whole new suite of radiation environments. This radiation will stem from the solar particles emanating from Proxima Centauri, Alpha Centauri 1, and Alpha Centauri 2, trapped radiation belts around planets with magnetic cores, and possibly unknown factors. Upon reaching the Proxima Centauri system, the probe will still be traveling at  $0.2c$ , which means it will not be subject to this local radiation environment for long. However, this environment should be researched and its effects on the spacecraft considered before launch. Doing so will require a stronger knowledge of the Proxima Centauri star system, its orbiting bodies, and its stars' solar activity. This literature review and simulation did not explore the radiation from this environment.

## 2.2 Quantifying Radiation

In order to understand specific effects of radiation on materials, there are standard methods that exist to quantify radiation. This section presents those methods, along with calculations and key ideas that will manifest in Chapter 3 when discussing an applied simulation of the radiation for Starshot.

### 2.2.1 Classifying Radiation

The ability to classify and quantify types of radiation impacting the Starshot probe is important for understanding the material and electronics effects on the spacecraft. As mentioned previously, this study focuses on particle radiation, not EM radiation.

Particle radiation is generally classified as either non-ionizing or ionizing, depending on its ability to ionize an electron from atoms in its path [43]. This distinction is a function of a variety of factors, but most importantly the particle's kinetic energy and charge. Understanding whether a particle is ionizing or non-ionizing is critical because it determines the dominant mode of interaction between the particle and the stopping medium.

When traveling with ionizing energies, particles interact with a target primarily via inelastic electronic interactions. Whether or not the incoming particle has a charge prior to entering the target, its high energy will quickly facilitate ejection of its outer electrons as it passes through the material, resulting in a charge on the incident particle. As the charged particle penetrates the target, energy is transferred to the target through the electric interaction of the particle's charge and electrons in the target [44].

Non-ionizing particles primarily interact with the target through nuclear forces and collisions between the incoming particle and nuclei in the target. These collisions can completely eject an atom from its spot in the substrate lattice, resulting in either a vacancy or an interstitial atom at another location. The collisions also have the ability to cascade, resulting in secondary collisions that occur off the main path. The different interaction characteristics of ionizing and non-ionizing particle radiation are visualized well in Figure 2.4.

The distinction between a non-ionizing and ionizing particle is technically dependent on the target material it interacts with because the target's composition determines the energy at

which electrons within it will be ionized. However, we can establish a standardized energy cutoff between ionizing and non-ionizing particles at around 100 keV, which is orders of magnitude larger than the binding/ionization energies for outer electrons of every element [45]. As shown in Table 2.3, the energy of all particles considered in this radiation study is on the order of MeV, so we will only consider ionizing radiation effects for the remainder of this paper.

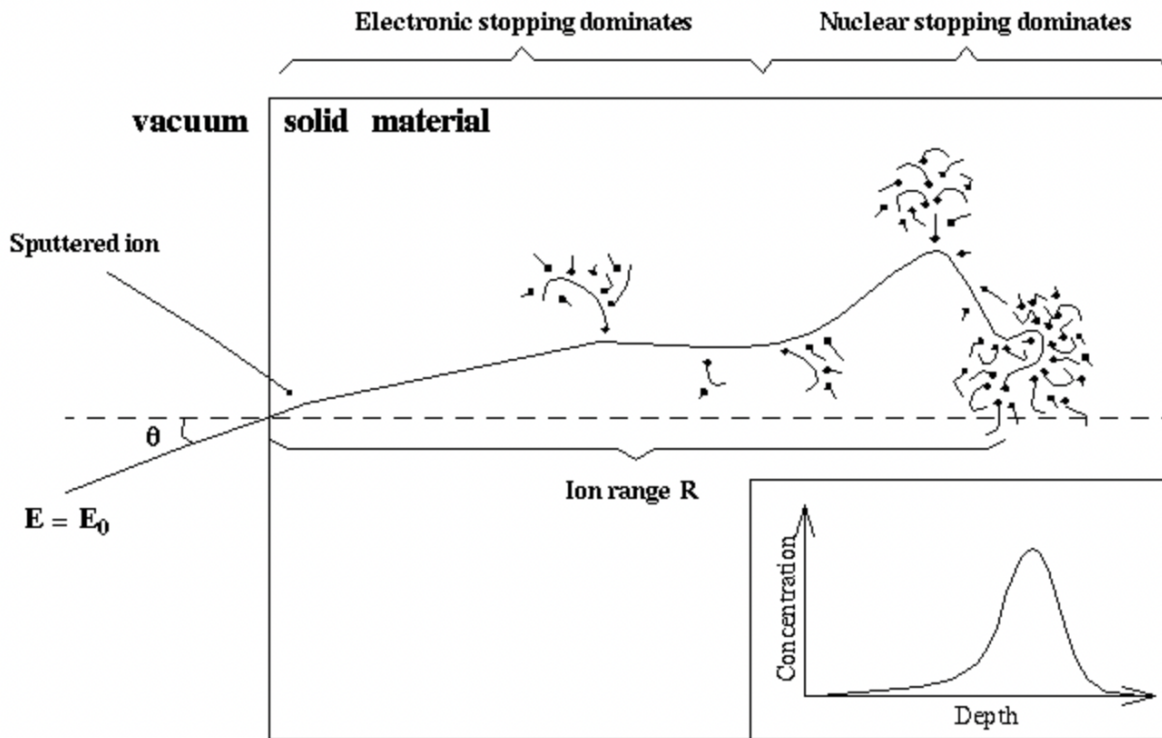


**Figure 2.4:** A 2-D visual of the interaction between an incoming particle and a target material. The particle enters the target at ionizing energies, therefore it initially interacts with the substrate through electronic interactions which do not significantly change its trajectory. After depositing energy into the target, it eventually slows down and possesses only non-ionizing energy. Thereafter, the particle interacts with the target mainly through nuclear forces and collisions, which redirect the particle and cause cascading effects. Upon losing all of its kinetic energy, the particle is deposited at a certain depth in the material. The inset plot shows that for a given incident particle energy, one can create an expected distribution of ranges at which the incident particle will be deposited in the substrate. Figure reproduced from Kai Nordlund [46].

A key quantity used to anticipate radiation effects in a material is stopping power.

Stopping power, normally expressed in units of  $\frac{MeV \cdot cm^2}{g}$ , reflects the amount of energy that an incoming particle will pass to a target medium as it penetrates it [47]. By multiplying stopping power by the density of the target material, one can determine a quantity with units  $\frac{MeV}{cm}$ , which

is the amount of energy absorbed by the target for each unit of distance the particle penetrates into the target, known as Linear Energy Transfer (LET). It is important to note that stopping power is generally a positive quantity, with its magnitude being equal to both the amount of energy gained by the target and the amount of energy lost by the incident particle. A stopping power curve, an example of which is shown in Figure 2.5, plots instantaneous stopping power of a particle versus instantaneous kinetic energy of a particle. As the kinetic energy of a particle changes, so too does its stopping power.

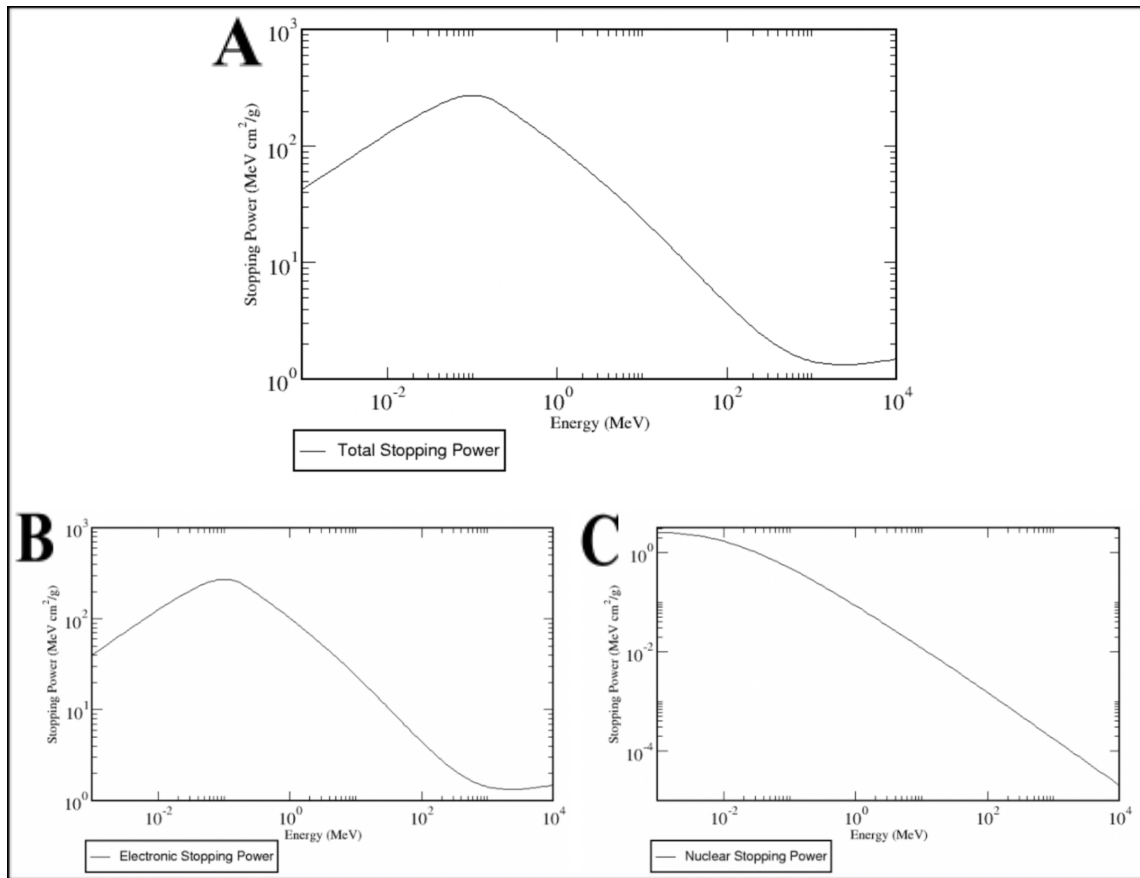


**Figure 2.5:** Stopping power curves for protons in a molybdenum target. **(A)** Total stopping power, incorporating both electronic and nuclear interactions. **(B)** Electronic stopping power, reflecting only electric interactions between the particle and the target. **(C)** Nuclear stopping power, reflecting only nuclear interactions and collisions between the particle and the target. Notice that even at the leftmost side of the x-axis, around 1 keV, electronic stopping power dominates the total stopping power. Figure adapted from NIST [48].

Stopping power is a superposition of both electronic and nuclear stopping power.

Electronic stopping power is dominant for ionizing radiation (incident particles with energies

above outer electron binding energies) and nuclear stopping power is dominant for non-ionizing radiation (incident particles without enough energy to ionize electrons in the target). For the purpose of this study, we use electronic stopping power as an approximation of total stopping power because the energy of the particle radiation found in space is many orders of magnitude above the threshold that distinguishes nuclear and electronic stopping power.

## 2.2.2 Stopping Power of Ionizing Particles

In order to simulate the effects of ionizing particles on superconducting nanowires, we require an equation that can compute the stopping power of a certain particle against a target material. In 1913, Niels Bohr presented the first equation to model the stopping power of a heavy ionizing particle against a target material, shown in Equation (2.3) [44, 49]:

$$\frac{dE}{dx} = \frac{4\pi z^2 e^4 n}{mV^2} Z \ln\left(\frac{1.123mV^3}{ze^2 \omega}\right). \quad (2.3)$$

In his formulation, Bohr considers classical effects that cause stopping power. Hans Bethe later presented a relativistic consideration of stopping power, shown in Equation (2.4) [49, 50]:

$$\frac{dE}{dx} = \frac{4\pi z^2 e^4 n}{mV^2} Z \left( \ln \frac{2mV^2}{I(1-\beta^2)} - \beta^2 \right). \quad (2.4)$$

Bethe incorporates a relativistic effect,  $\beta$ , along with a parameter for the excitation potential of the target medium,  $I$ . Eqs. (2.4) and (2.5) are the basis for the more unified Bethe-Bloch equation, Equation (2.6):

$$- \left| \frac{dE}{dx} \right| = KZ^2 \frac{Z}{A^2 \beta^2} \left[ \frac{1}{2} \ln \frac{2m_e c^2 \beta^2 \gamma^2 T_{max}}{I^2} - \beta^2 - \frac{\delta(\beta\gamma)}{2} \right], \quad (2.6)$$

where

$$T_{max} = \frac{2m_e c^2 \beta^2 \gamma^2}{1 + \frac{2\gamma m_e}{M} + \left(\frac{m_e}{M}\right)^2}. \quad (2.7)$$

The Bethe-Bloch equation is currently accepted and utilized for calculating stopping powers of ionizing, heavy particles impacting matter [47]. This equation is used for simulations in Chapter 3.

**Table 2.4:** Parameters and variables used in the Bethe-Bloch electronic stopping power formula Eqs. (2.6) and (2.7) [47].

<u>Symbol</u>	<u>Definition</u>	<u>Units or Value</u>
$K$	–	$0.307075 \text{ MeV} \cdot \text{cm}^2 \cdot \text{g}^{-1}$
$z$	Charge of incident particle	–
$Z$	Atomic number of absorber	–
$A$	Atomic mass of absorber	$\text{g} \cdot \text{mol}^{-1}$
$\beta$	Fraction of speed of light, $\frac{v}{c}$	–
$m_e c^2$	Electron mass $\times c^2$	$0.510999 \text{ MeV}$
$\gamma$	As defined in Eq. (2.2)	–
$I$	Mean excitation energy of absorber	$eV$
$\delta(x)$	Density effect correction	See Eq. (2.8)
$M$	Incident particle mass	$\text{MeV} \cdot c^{-2}$

Equation (2.8) is used to determine the density effect correction to stopping power, which is important at extremely high particle energies, above GeV [47]. Parameters in the equation are dependent on the target material, and are presented in [51] from theory and empirical data.

$$\delta(\beta\gamma) = \begin{cases} 2(\ln 10)x - \overline{C} & \text{if } x \geq x_1; \\ 2(\ln 10)x - \overline{C} + a(x_1 - x)^k & \text{if } x_0 \leq x < x_1; \\ 0 & \text{if } x < x_0 \text{ (nonconductors);} \\ \delta_0 10^{2(x-x_0)} & \text{if } x < x_0 \text{ (conductors)} \end{cases} \quad (2.8)$$

The result of the Bethe-Bloch equation is a number,  $-\left|\frac{dE}{dx}\right|$ , where  $E$  is the energy of the incident particle and  $x$  is depth in the target material. The term  $\left|\frac{dE}{dx}\right|$  represents the mean rate of energy loss of the incident particle as it travels through the medium, in units of  $\frac{\text{MeV}\cdot\text{cm}^2}{\text{g}}$ .

Negating this number yields the mean rate of energy absorption by the medium, which is termed “stopping power.” As mentioned in Section 2.1.1, multiplying this form of stopping power by the density of the target medium results in a more useful expression with units of energy per unit traveled. Stopping power in this form,  $\frac{\text{MeV}}{\text{cm}}$ , is easily used to determine radiation effects such as total absorbed dose and specific doses from particular particles.

Equation (2.6) is used for determining the stopping power of a particle in a single-element target, but it doesn’t support direct computation of the stopping power of a projectile in a compound. Since the superconducting materials we consider are compounds, such as NbN, MoSi<sub>2</sub>, or WSi<sub>2</sub>, we need to apply the Bragg Additivity Rule in order to compute stopping power in a compound. This rule states that the total stopping power of a compound can be estimated as a linear combination of the stopping powers of its individual elements, where an element’s contribution to the total is weighted by its mass fraction of the compound [52, 53].

Bragg’s Rule is shown in Equation (2.9):

$$S = \sum_j w_j S_j, \quad (2.9)$$

where  $S$  is stopping power and  $w_j$  is the mass fraction of the  $j^{\text{th}}$  atomic constituent.

In the following chapter, I use the stopping power and additivity equations presented in this section to create a numerical simulation of various radiation effects anticipated in the electronics onboard a Starshot probe.

## **3 Effects of Radiation on Superconducting Electronics**

It is important to understand how radiation in space, and in other environments, affects superconducting electronics. Superconductivity in devices predisposes them to a sensitivity towards temperature, magnetic field, and various other factors. Though this sensitivity can be harnessed to create electronics and devices, it also increases susceptibility towards uncontrolled electronic disturbances. We must understand the undesired effects of environmental conditions, particularly radiation, on superconducting electronics in order to correct for them and design resiliency in devices.

### **3.1 Starshot Radiation Model**

We present a general model for simulating impacts of particle radiation with a Starshot probe along its journey to the Proxima Centauri star system. For this model we required 3 components: information on the particle radiation environment, structural detail of the radiation target (the sailcraft's electronics), and a method to quantify interaction between the two. In this section, I describe the process of combining these three components and present relevant results for understanding effects of radiation on the superconducting electronics onboard.

#### **3.1.1 Simulation Setup and Model**

The first component in simulating radiation effects for Starshot was an accurate model of the radiation environment through which the probe will pass. For this simulation, we used the radiation parameters presented in Table 2.3, which were the result of a literature review of the anticipated deep space radiation environment. This information includes particle type, charge, flux, and energy of interstellar radiation.

Next, we modeled the radiation target – the sailcraft's electronics. While there is uncertainty in exactly which materials would be used for onboard superconducting electronics, we designed the simulation to support NbN, MoSi<sub>2</sub>, WSi<sub>2</sub>, Si, SiO<sub>2</sub>, and graphite. To account for multi-layered electronics, we modeled the target as a layered structure of different materials.

Each layer is defined along with its surface area and thickness, which are used to determine the number of incident particles. We assumed all particles were incident normal to the surface of the target.

With the environment and target modeled, we simulated interactions between the two using Equation (2.6), the Bethe-Bloch electronic stopping power formula. The result of this equation is a value for the stopping power of a specific particle within a given target layer. We did not enforce that layers in the target consist of pure elements. By using the Bragg Additivity Rule shown in Equation (2.9), we computed electronic stopping power for compounds. We also needed to retrieve density effect parameters and mean excitation energy from [51] for each element in the target. Figure 3.1 shows the general setup: various particles incident on a layered target, with stopping power computed for each particle-layer combination.

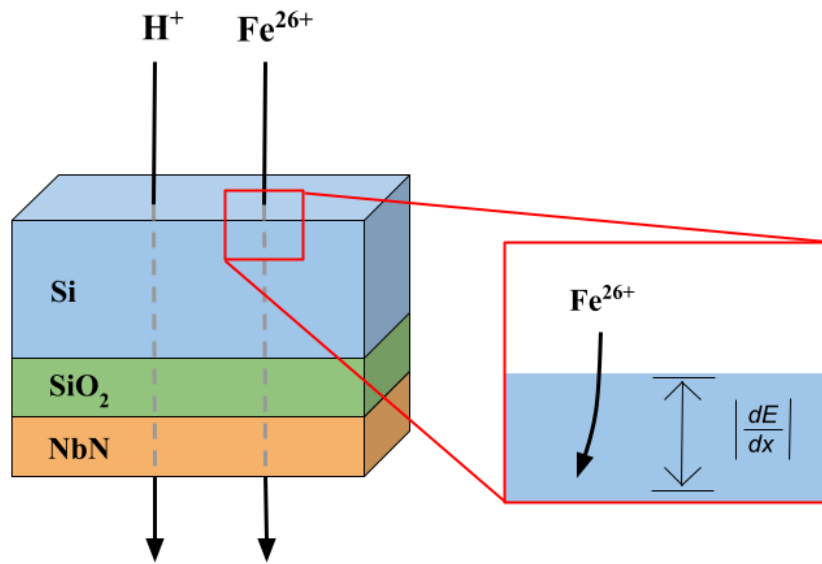


**Figure 3.1:** A visual of the simulation process for particle radiation impacting a Starshot sailcraft. In this example, the radiation environment consists of H<sup>+</sup> and Fe<sup>26+</sup> ions that impact a surface composed of three layers. The magnified region on the right depicts the calculation of electronic stopping power as a Fe<sup>26+</sup> ion penetrates the Si layer.

With the ability to calculate stopping power for any incoming charged particle on any layered target, the simulation supports calculations of various effects of radiation such as total dose, energy deposited by a single particle, comparison of energy deposits from various particles, and filtering of events within a certain energy threshold. The pseudocode for calculation of a

total ionizing radiation dose on a layered target from an assortment of incoming particles is shown in Figure 3.2. Adjustments to this pseudocode easily allow for calculation of the other effects mentioned above.

```
total_dose = 0
for particle in particle_assortment:
    for layer in target:
        S = stopping_power(particle, layer)
        dose = S · flux · area · thickness · duration
        total_dose += dose
print(total_dose)
```

**Figure 3.2:** Pseudocode for the calculation of a total ionizing radiation dose on a layered target from a collection of particles. Stopping power is computed separately for each particle-layer combination. The dose of a given particle-layer pair is determined not only by stopping power, but also by the particle flux, layer area, layer thickness, and duration of exposure.

Since electronic stopping power is a function of the incident particle’s velocity, we do incorporate a small error because this simulation assumes that particle velocity is constant for the duration of its trajectory through the target. This assumption is valid in our case because the incident particle energy is many magnitudes larger than the amount of energy deposited in the nm-thick sailcraft, as is shown in Section 3.1.1. A more robust simulation would account for energy losses of the particle and recompute electronic stopping power at small increments of depth within the target.

### 3.1.1 Simulation Results

In order to verify the calculations of electronic stopping power from Equation (2.6), it was necessary to compare computed stopping power graphs from our simulator against accepted data from the National Institute of Standards and Technology (NIST). By doing so for multiple particle types (protons and alpha particles) and both single-element and compound targets, we verified our calculations of electronic stopping power were valid, including calculations using the Bragg Additivity Rule, Equation (2.9). Figure 3.3 presents a comparison between our calculated electronic stopping power graphs and the data from NIST.

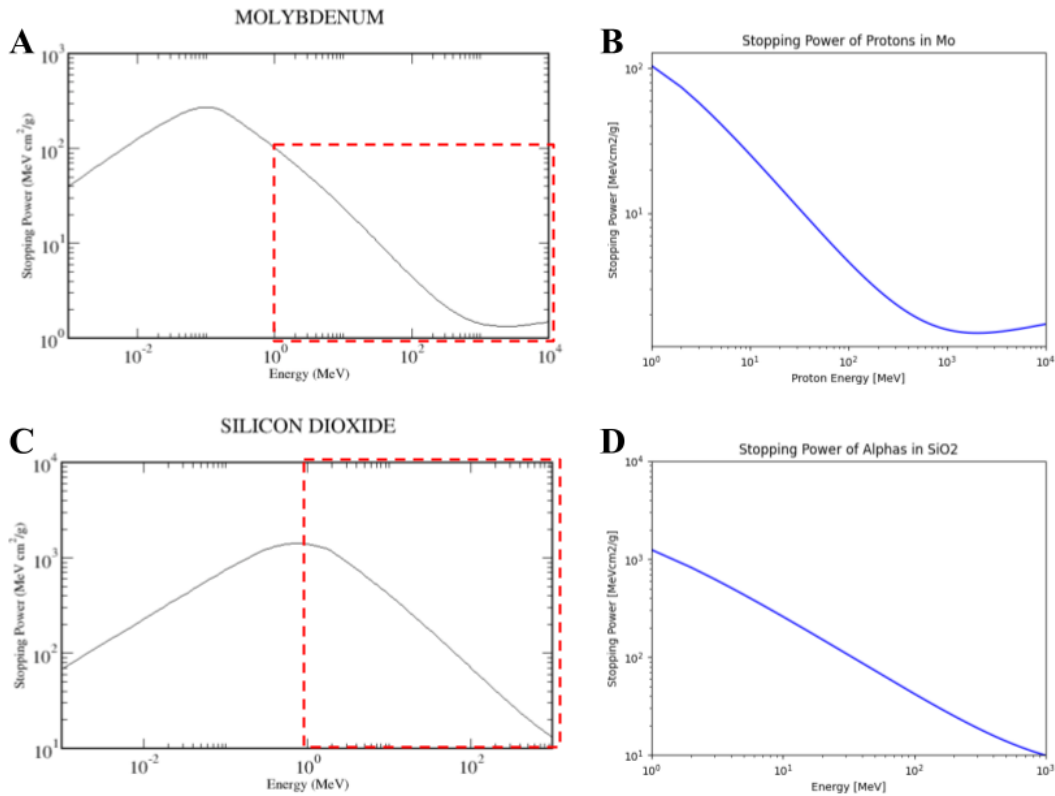


**Figure 3.3:** Comparisons between NIST electronic stopping power graphs (left) and our calculated electronic stopping power graphs (right). **(A)** NIST electronic stopping power graph of a proton in a molybdenum target. A dashed red box outlines the limits used in our graph on the right. **(B)** Our calculated electronic stopping power graph of a proton in a molybdenum target. **(C)** NIST electronic stopping power graph of an alpha particle in a silicon dioxide target. A dashed red box outlines the limits used in our graph on the right. **(D)** Our calculated electronic stopping power graph of an alpha particle in a silicon dioxide target. The shoulder from the NIST data at 1 MeV is not evident in our plot, but the magnitudes across the entire energy spectrum are nearly identical.

Knowing that our calculations of electronic stopping power were valid for various incoming particle types and compound targets, we then calculated the total ionizing radiation dose in the onboard electronics. We did so for two different sailcraft configurations: face-on and side-on. In the face-on configuration, the sail is not rotated after the propulsion stage, so its cross sectional area as it traverses the interstellar medium is the entire area of the sailcraft (~15 m<sup>2</sup>). Onboard electronics may be concentrated within a 1 cm<sup>2</sup> area either within the sail or suspended behind it. In the side-on configuration, the sail is rotated so that its cross sectional area as it traverses the interstellar medium is significantly reduced. In the side-on configuration, the cross sectional area is the sail's width multiplied by its thickness. Although these dimensions are

unknown currently, the Starshot Requests for Proposals document for the communications subgroup stated that a sail width of 4 m and sail thickness of 100 nm should be anticipated. In the side-on configuration, we assumed the electronics would be at the rear end of the sailcraft, contained within a 1 cm<sup>2</sup> area. Figure 3.4 depicts the geometric assumptions for the calculations of total dose.

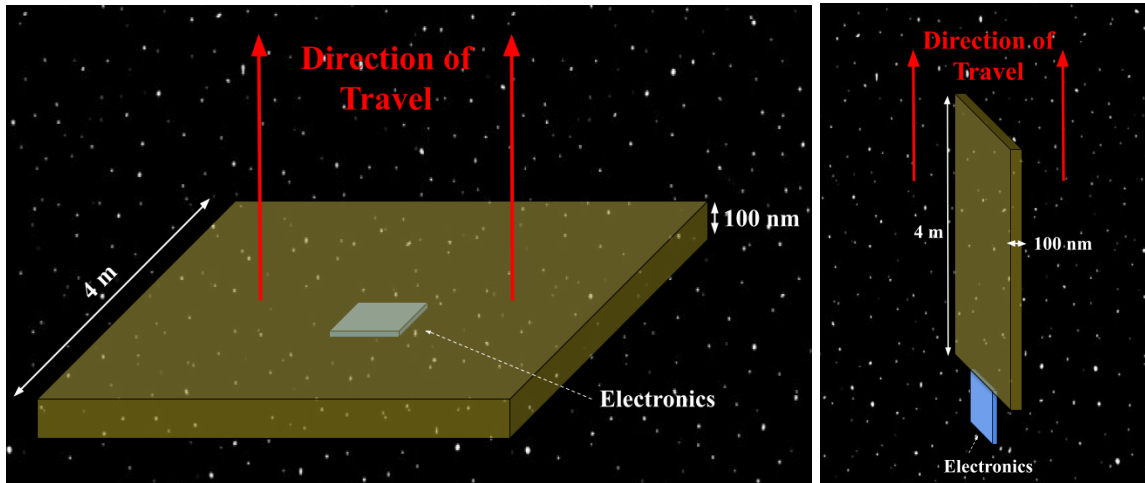


**Figure 3.4.** Left: The face-on configuration for transit of a Starshot lightsail. In this configuration, the majority of the sail’s surface area is perpendicular to the direction of travel. For calculations of total dose with this configuration, we assumed electronics are housed in a 1 cm<sup>2</sup> area on the backside of the sail. Right: The side-on configuration for transit of a Starshot lightsail. In this configuration, the majority of the sail’s surface area is parallel to the direction of travel. For calculations of total dose with this configuration, we assumed electronics are housed in a 1 cm<sup>2</sup> area at the bottom of the sail. These drawings are not to scale.

For both configurations, we assumed a 25-year exposure to the radiation shown in Table 2.3, where the H<sup>+</sup> interstellar gas particles collide only from the front, but the remaining particles from cosmic radiation are omnidirectional. In both configurations, we calculate only the total dose within the 1 cm<sup>2</sup> area that contains the material for superconducting electronics. We considered two different structures for the 1 cm<sup>2</sup> superconducting electronics: a single layer of NbN and a layer of NbN on top of SiO<sub>2</sub> substrate. These geometries are shown in Figure 3.5. Although we only present results for two configurations of superconducting electronics, the simulation is designed to produce results for any structure composed of NbN, MoSi<sub>2</sub>, WSi<sub>2</sub>, SiO<sub>2</sub>, or Si.

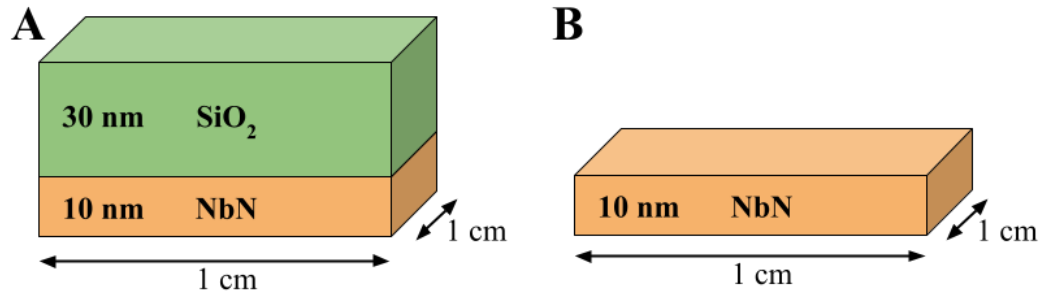


**Figure 3.5.** Geometries of superconducting materials for Starshot radiation simulation. **(A)** Two-layer geometry consisting of a SiO<sub>2</sub> substrate and NbN superconducting layer. **(B)** One-layer geometry of a NbN superconducting layer.

The total dose calculations for both sailcraft configurations and both electronic layer configurations are presented in Table 3.1. It is important to note that in the edge-on configuration, the electronics are effectively shielded from collisions with interstellar gas (H<sup>+</sup> particles). These particles will either be deposited at some depth within the 4 m sail or will be deflected outwards into space due to electronic deflection. More research needs to be conducted to determine the fraction of incoming interstellar dust that would deposit within the sailcraft versus deflect outwards into space. Future research into the sailcraft design should also look at using shielding on the leading edge in the edge-on configuration. This is discussed briefly in [16].

**Table 3.1.** Total ionizing radiation dose calculations for face-on vs. side-on sail configuration and single vs. double layer electronic configuration. Calculations are for a 25 year mission in interstellar space. Incoming radiation is presented in Table 2.3.

	<u>Face-On Sail</u>	<u>Edge-On Sail</u>
<u>Single Layer Electronics</u>	2.05 × 10 <sup>20</sup> eV	3.53 × 10 <sup>9</sup> eV
<u>Double Layer Electronics</u>	4.61 × 10 <sup>20</sup> eV	7.66 × 10 <sup>9</sup> eV

There is an incredible difference in the amount of energy absorbed in onboard electronics between the edge-on and face-on design. This is because the sail structure serves as shielding against interstellar gas in this configuration. Table 3.2 shows the breakdown in energy absorbed

from each particle in Table 2.3 for the single layer face-on design. It is evident from this table the magnitude at which interstellar dust deposits energy into the onboard electronics.

**Table 3.2.** Total ionizing dose from each particle type of incoming radiation. These numbers were calculated for the face-on single layer configuration exposed to 25 years of radiation. The effect of interstellar gas ( $H^+$  particles) is many magnitudes larger than any other particle.

<u>Particle Type</u>	<u>Total Dose</u>
Proton	$1.86 \times 10^9 \text{ eV}$
$H^+$	$2.05 \times 10^{20} \text{ eV}$
$He^{2+}$	$1.21 \times 10^9 \text{ eV}$
$C^{6+}$	$2.43 \times 10^8 \text{ eV}$
$Fe^{26+}$	$2.19 \times 10^8 \text{ eV}$

These calculations of total radiation dose are valuable because they give us a benchmark for testing the superconducting materials. By exposing a similar structure of superconducting electronics to an equivalent radiation dose on Earth, then measuring their superconductivity and electrical parameters, we can determine whether gradual degradation in space will cause electronic failure or not. I have been pursuing neutron irradiation studies for NbN and other superconducting materials at the MIT Nuclear Reactor test facility in order to get a sense of the impact of high radiation doses on the basic superconducting properties of thin-film superconductors. Although I am not prepared to present the results in this thesis, I hope they prove valuable to understanding operation of superconducting devices in high radiation environments.

Another interesting calculation related to total dose is the expected change in sailcraft velocity due to collisions with interstellar radiation along its voyage. Using the classical kinetic energy equation with a sailcraft mass of 3.6 g and a velocity of  $0.2c$ , we find the kinetic energy of the sailcraft upon launch is roughly  $4.0 \times 10^{31} \text{ eV}$ . Using our radiation simulator for a 100 nm x 4 m x 4 m graphite sail exposed to interstellar radiation for 25 years, we calculated a total ionizing dose of  $7.69 \times 10^{25} \text{ eV}$ . This number is dominated by the electronic stopping power of interstellar gas particles that impact the sail along its direction of motion; the collisions and their

cumulative energy slow down the spacecraft. However, the amount of energy lost from these interactions is six orders of magnitudes smaller than the initial kinetic energy of the sail, so we do not anticipate any noticeable decrease in velocity. In reality, we may very well find that the sailcraft does slow down after launch due to variations in the density of the interstellar medium, which may be quite dense in some regions. This project offers a vantage from which we can more accurately study the composition of the interstellar medium in general.

In addition to considering total radiation dose in the electronics onboard, we also assessed transient errors in electronics that could arise due to radiation. We do expect there to be transient errors due to radiation in an unshielded, unmodified layer of superconducting electronics. These transient errors are the result of energy deposits as ionizing radiation passes through a section of superconducting nanowire. The process of error formation is discussed more thoroughly in Section 3.2. Each interaction between an ionizing space particle and the superconducting layer will deposit enough energy to create an error in the electronics, so the anticipated error rate is identical to the cumulative flux rate of all expected particle radiation through the electronics. This rate is dependent on sailcraft configuration. The anticipated particle flux rate, and error rate, through the electronics in a face-on configuration is  $1.8 \times 10^{-7} \frac{\text{errors}}{10 \text{ ns} \cdot \mu\text{m}^2}$ . The anticipated particle flux rate, and error rate, through the electronics in a side-on configuration is  $1.23 \times 10^{-17} \frac{\text{errors}}{10 \text{ ns} \cdot \mu\text{m}^2}$ . The flux rate in the side-on configuration is much smaller because of the sailcraft's shielding against interstellar gas. A period of 10 ns was chosen to correspond with a clock frequency of 100 MHz, but the error rate can be scaled up or down depending on actual operating frequency. The number of errors is shown in terms of  $\mu\text{m}^2$  because that is the approximate area of a superconducting device such as an nTron [12].

This simulation provides first order estimates of the quantity of radiation expected in the electronics of a Starshot probe. However, it will need to be modified as mission parameters are finalized, such as sailcraft orientation, sailcraft area, clock frequency of electronics, and location of electronics onboard the sail.

## 3.2 Effects of Radiation on Superconductivity of Nanowires

Now with a method to quantify the energy and frequency of interactions between radiation and the sailcraft, it was important to assess the effects of radiation on the superconductivity of nanowires. Specifically, how radiation could interrupt logic in an entirely superconducting processor. It is with an understanding of these effects that we were able to develop a technique to mitigate undesired effects of radiation on superconducting devices, which is presented in Chapter 4.

### 3.2.1 Breaking of Superconductivity

The primary effect we anticipate in superconducting nanowires exposed to radiation is the formation of normal state, resistive regions (also called hotspots). Superconductivity in nanowires can be broken in various manners such as exceeding the critical current, critical temperature, critical magnetic field, or directly breaking Cooper pairs [54]. Although these conditions are normally considered separately, the boundary between the superconducting state and the normal state is a function of all of these.

We anticipate incidents where a highly energetic particle in space impacts a region of superconducting nanowire to create a normal area by directly breaking Cooper pairs using the energy absorbed in the nanowire from electronic stopping power. The process of forming a hotspot by breaking Cooper pairs is explained well in [54], which I will summarize here. The process begins when an incident particle makes contact with a superconducting nanowire. This interaction deposits energy in the nanowire, either by absorption (in the case of a photon) or by stopping power (in the case of a particle with mass). This surplus of energy in the superconductor breaks Cooper pairs, which have a binding energy  $E_b = 3.528 \cdot k_B \cdot T_c$ , where  $k_B$  is the Boltzmann constant and  $T_c$  is the critical temperature of the superconductor. If  $N \cdot E_b$  energy is deposited, for example, then roughly  $N$  Cooper pairs are broken. As a superconducting nanowire is biased with a current close to its critical current, it becomes sensitive to the breaking of Cooper pairs. As an example metric, NbN SNSPDs are sensitive to 1550 nm photons [55]. For NbN, with a  $T_c$  of 16 K,  $E_b = 6.4 \text{ meV}$ . A photon with a wavelength of 1550 nm has

$E_{\text{photon}} = 0.8 \text{ eV}$ . When a 1550 nm photon is absorbed in a NbN superconducting nanowire, roughly  $0.8 \text{ eV} \div 6.4 \text{ meV} = 125$  Cooper pairs are broken. This is suitable to create a hotspot in the nanowire and redirect current to a readout device for single photon detection. Figure 3.6 depicts the hotspot formation process from particle absorption.

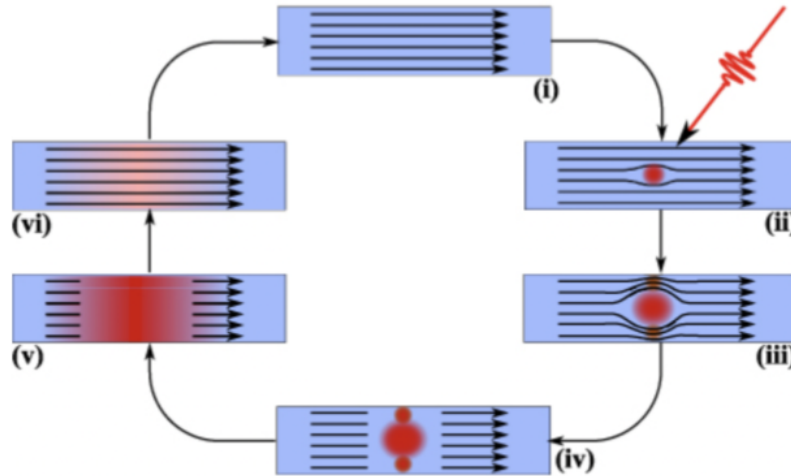


**Figure 3.6.** Hotspot formation process from an incoming photon. (i) The superconducting nanowire is in a superconducting state with current flowing through it. (ii) A photon impacts and is absorbed in the nanowire, breaking Cooper pairs in the local area where it was absorbed. (iii) Current redirects around the local area where the photon was absorbed and Cooper pairs were broken. (iv) The entire width of the wire switches to a normal state because the critical current density of the nanowire is exceeded as current is forced away from the area where the photon was absorbed. (v) The hotspot grows due to Joule heating from the normal region, which further breaks superconductivity. (vi) After current has been redirected elsewhere in the circuit - away from the hotspot in the nanowire - the temperature of the region drops below the critical temperature of the superconductor, allowing the device to return to a superconducting state. Figure reproduced from [56].

We anticipate unexpected and unpredictable hotspots to form in superconducting nanowire devices in space via a similar mechanism as in SNSPDs, where instead the incoming particle is either a cosmic ray or interstellar gas. The amount of energy deposited in a 10 nm thick layer of NbN from every type of interstellar radiation is presented in Table 2.3. Every instance of a particle in space interacting with a region of superconducting nanowire will deposit enough energy to break thousands of Cooper pairs.

This description of hotspot formation from the breaking of Cooper pairs does not consider the effects of particle absorption in the substrate, which may also cause local heating and suppress superconductivity that way. A more thorough analysis should be performed to

understand the impact of substrate on this mechanism, specifically for heavy ionizing particle radiation.

**Table 3.3.** Energy deposited in a 10 nm layer of NbN from a single particle. Calculated for each dominant particle type in space, using electronic stopping power. We assume the particle is incident normal to the surface of the NbN.

<u>Particle Type</u>	<u>Energy Deposited from Single Incident</u>
Proton	22.5 eV
H <sup>+</sup>	144.6 eV
He <sup>2+</sup>	90.0 eV
C <sup>6+</sup>	669.7 eV
Fe <sup>26+</sup>	10,402 eV

### 3.2.2 Impact on Electronics

In the case of detectors, such as SNSPDs, hotspot formation along a superconducting nanowire is desired and necessary for operation. Superconducting logic elements also operate through the use of hotspot formation, but only in very specific regions of the device where an input signal triggers a normal state. While properly operating nTrons and hTrons, the device only ever forms a hotspot in the region where the gate meets the channel [12, 13]. Undesired hotspot formation outside this region, without an input trigger, could cause a false output. Figure 3.7 depicts how an incident particle in space could trigger a false output of an nTron. In this figure, a Fe<sup>26+</sup> ion collides with the channel of an nTron, creating a hotspot. This redirects current to some output in the same process that would occur if an input signal were sent through the gate. Since no input was sent to the gate however, this event would cause a false output. False firings like this can occur for nTrons, hTrons, SNSPDs, and any other superconducting nanowire device that relies on hotspot formation from a specific event. Errors may also occur in cascaded superconducting logic, which is explained further in Chapter 4.

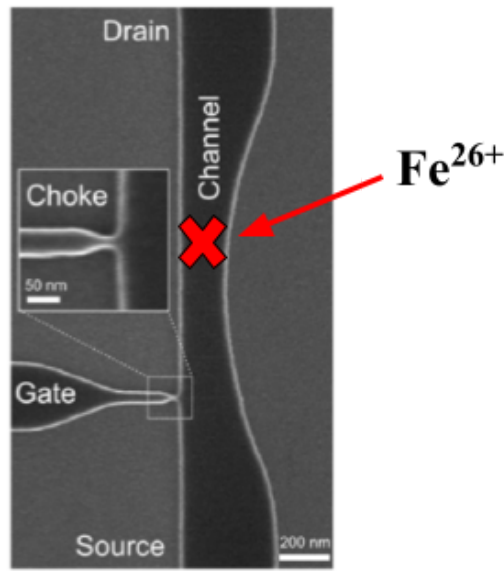


**Figure 3.7.** Hotspot formation in the channel of a nTron due to a collision with an iron ion, which deposits enough energy to break Cooper pairs and form a normal region. An incident like this would cause current to redirect from the channel to an output, leading to a false output since the gate did not receive any signal. Figure reproduced from [12].

Operation of superconducting nanowire devices in the presence of ionizing radiation makes them susceptible to transient errors arising from unexpected hotspots and normal regions that form within the device as a result of interaction with incoming particles.

### 3.3 Heating of Sailcraft

In addition to causing transient electrical errors in superconducting circuits and imparting a total radiation dose on the sail and electronic material, constant interstellar gas bombardment deposits a time-averaged power that heats the sailcraft above the ambient temperature in space, which is around 3 K [57].

This heating effect was assessed by Hoang, et al. in [41]. In their assessment, they calculated average sailcraft temperature by balancing the heating from interstellar gas interactions with radiative cooling from the sail. Part of their assumption was that the cross sectional area for interaction with the interstellar medium was the same area that emitted gray-body cooling radiation. This assumption is accurate for the face-on configuration, shown in Figure 3.4. The results of their sailcraft temperature calculations, as a function of sail speed and

interstellar gas density, are shown in Figure 3.8. This work is valuable because the face-on configuration is a possible method of transit, particularly if a high average sail temperature is needed for electronics, power generation, or some other reason. It is also valuable because it visualizes the effect of traveling through regions of interstellar space with different gas densities, because we may find that the space between our Sun and Proxima Centauri is not very homogeneous.

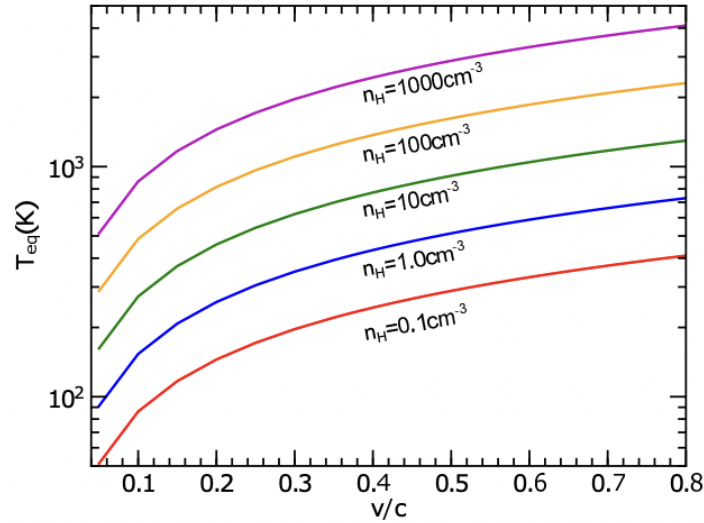


**Figure 3.8.** Calculations of average sailcraft temperature for the face-on configuration. Temperature is plotted as a function of sail velocity. Different curves are plotted to represent different interstellar gas densities that the probe may travel through, with the highest density leading to the warmest sailcraft. Figure reproduced from [41].

We can perform a similar calculation of the average sailcraft temperature for the edge-on configuration, which accounts for a different cross sectional collision area and radiative area. To do so, we first create an expression for the average power deposited into the sailcraft by interstellar radiation. Since interstellar radiation incident with the sailcraft is dominated by gas, we consider only those collisions in this calculation. This calculation of average power absorbed by the spacecraft is shown in Equation (3.1):

$$P_{abs} = A_{collision} \cdot \Phi_{gas} \cdot E_{gas} \cdot d_f, \quad (3.1)$$

where  $P_{abs}$  is the time-averaged power absorbed by the sailcraft from interstellar gas,  $A_{collision}$  is the cross section of the sailcraft as it travels,  $\Phi_{gas}$  is the flux of interstellar gas,  $E_{gas}$  is the energy of the incident gas particles, and  $d_f$  is a deflection factor  $\leq 1$ . For the edge-on case,  $d_f$  may be important because electronic deflection inside the sail could prevent complete stopping of every incident gas particle. For our calculations, we assume this to be 1, but it is almost certainly less than 1. Also for our calculations, we assume complete stopping of each incident gas particle. Without a complete stopping graph that includes nuclear stopping power, we cannot say this for certain; but in this calculation we are assuming the worst case scenario, where all energy from incident interstellar gas is deposited into the sail. From Table 2.3, we can populate the variables in Eq. (3.1):  $\Phi_{gas} = 1.8 \times 10^{13} m^{-2} s^{-1}$  and  $E_{gas} = 38 MeV$ . From the dimensions in Figure 3.4,  $A_{collision} = 4 \times 10^{-7} m^2$  for the edge-on case. This yields a value for the average power absorbed of  $P_{abs} = 2.73 \times 10^8 MeV \cdot s^{-1}$ .

Next, we use the gray-body radiation formula, Equation (3.2), to form an expression for the average power emitted,  $P_{emit}$ , by the sail as a function of sail temperature:

$$P_{emit} = \epsilon \cdot \sigma \cdot A_{radiative} \cdot (T_{craft}^4 - T_{ambient}^4). \quad (3.2)$$

Here,  $\epsilon$  is the emissivity of the sail's surface, which we estimate as 0.7.  $A_{radiative}$  is the surface area of the sailcraft that radiates heat into the environment. For the edge-on configuration, both of the sail's square sides radiate heat into the cosmos, so  $A_{radiative} = 32 m^2$ . The Stefan-Boltzmann constant,  $\sigma$ , is  $3.54 \times 10^5 MeV \cdot m^{-2} K^{-4} s^{-1}$ .  $T_{ambient}$  is the 3 K background temperature in deep space and  $T_{craft}$  is the equilibrium temperature of the spacecraft, which we are solving for.

Assuming a thermal equilibrium is reached within the sailcraft during its transit to Proxima Centauri, we can then equate Eq. (3.1) and Eq. (3.2) to solve for  $T_{craft}$ . When we do so, we arrive at an equilibrium sailcraft temperature of 3.28 K.

While this is a rough estimate, given the assumptions made about particle flux, stopping power, sail emissivity, and area of the sail, it does suggest a two-magnitude decrease in the expected sail temperature from [41] may be possible. If so, the door remains open to the usage of superconducting electronics with critical temperatures on the order of 10 K.

## 4 Design of Radiation-Hard Superconducting Electronics

For Breakthrough Starshot probes, or any other technical instrument that operates in a high radiation environment, we need support electronics that can operate despite environmental radiation. In most space applications, electronics are able to operate in the presence of radiation through a combination of radiation shielding on the craft and redundant electronic design on-chip [58]. While redundant electronic design has been researched and demonstrated for semiconductor-based electronics, it has yet to be purposefully investigated for superconducting electronics [59]. Although we are years away from fully superconducting microprocessors, this chapter presents the motivation and design of on-chip resiliency against errors in superconducting electronics from space radiation.

### 4.1 Motivation for Resilient Devices

Designing superconducting devices that are resilient against radiation effects is incredibly important for use on a Starshot sailcraft, where shielding is not an option due to mass restrictions. One can imagine that in twenty years, when the first Starshot probe launches, an onboard superconducting microprocessor may have millions of nanowire-based devices connected by superconducting interconnects. If such a chip were embedded within a Starshot lightsail, on-chip methods would need to be employed to minimize errors caused by the radiation events discussed in Chapter 3. With no possibility for repair once launched, and possibly no uplink to the spacecraft, the electronics on board must be able to locally handle any errors from radiation.

High-level methods can be employed to reduce the effects of radiation errors, such as duplication or triplication of logical processes. In such a scheme, identical logical operations are performed multiple times to verify the output is consistent. By pipelining logic with redundancy, errors can be dramatically reduced. However, this also increases power consumption for performing any redundant processes [59]. Low-level methods can also be used to reduce electronic radiation effects by redesigning device geometry to reduce susceptibility to impacts of ionizing radiation [60]. For a large superconducting microprocessor on-chip, composed of

nanowire devices and long interconnects, geometric modifications may reduce susceptibility to errors from radiation. For the research in this thesis, we focused on designing resilient superconducting interconnects to prevent errors from occurring along the many interconnects that will eventually be on-chip in a superconducting processor.

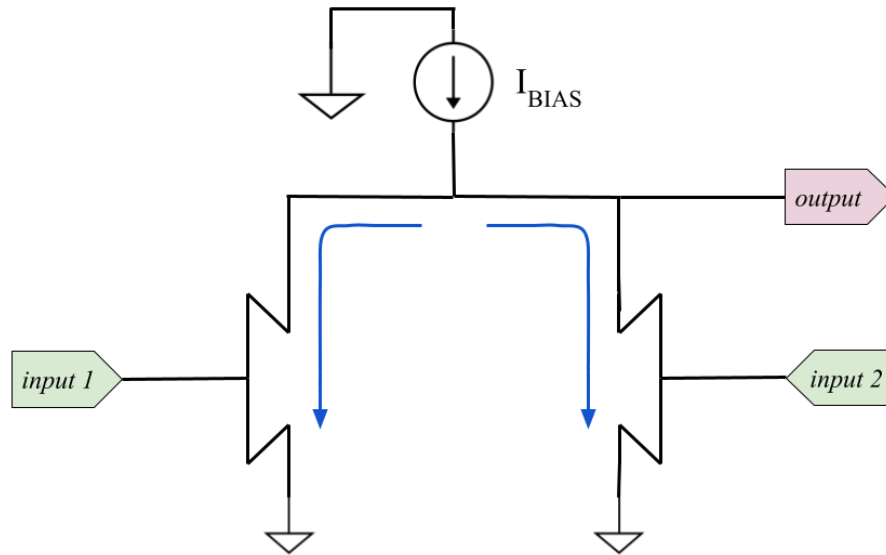
To further motivate the designing of resilient interconnects, and to expand upon the hotspot issue shown in Figure 3.7, we present schematics of a multi-device logical OR gate and a two-device cascade that demonstrate the susceptibility of interconnects to introducing radiation errors into superconducting electronics.

Figure 4.1 is the schematic of a superconducting OR gate, designed with two nTron devices [12]. The current source inductively splits between the two superconducting paths to ground, which biases each nTron near its switching current. When a suitable input is applied to the gate of either nTron, the device forms a highly resistive region in the channel, redirecting current to the other device. With nearly the entire bias current redirected to one side, the second device forms a hotspot in the channel as its switching current is exceeded. Now, with a hotspot in the devices on both sides, current is redirected to the output. This is the proper method for operating the OR gate.

Alternatively, radiation can cause an improper output on the OR gate. If ionizing radiation passes through an interconnect line feeding bias current into either device, it will deposit enough energy to create a hotspot at the area of collision. Once this hotspot forms in one branch, nearly the entire bias current is redirected towards the other device, causing it to switch and form a resistive region. With hotspots in both branches of the OR gate, current then redirects to the output. In this scenario, the OR gate resulted in a true output even though both inputs were false – radiation along the interconnect caused an erroneous output.

Figure 4.2 is the schematic of a cascade with two superconducting devices, to show another example of the impact of radiation on interconnects. Without any incidents of radiation, when an input current is injected into the gate of the left-most device, the device switches and redirects its entire bias current through an interconnect to the gate of the rightmost device. With a high signal on its gate, the device on the right then forms a hotspot in its channel, driving its bias current to the output. In this manner, the cascade functions as expected. If ionizing radiation passes through the interconnect line connecting the output of the left device to the gate of the right device, it will create a hotspot at the area of collision. This resistive hotspot will then create

a current divider between itself and the hotspot in the left device, reducing the current being delivered to the device on the right. In the case of pulsed logic, this may not be a terrible issue because the probability of an ionizing particle impacting the interconnect line at the moment it carries a current pulse may be negligible. However, for cascaded loads that require a constant input current, any incident radiation along the interconnect leading to it may prevent proper operation.



**Figure 4.1.** A nanowire-based superconducting OR gate. With no inputs, the bias current inductively splits between the left and right branches, as shown in blue. When the input on the gate of either device is fed with suitable current, the device switches into the resistive state, redirecting the bias current to the other branch. This then causes the other branch to break superconductivity because the critical current of the nanowire is exceeded. With normal regions in both branches, the current then redirects to the output. The interconnects between the bias source and the devices on either branch are susceptible to ionizing radiation. If radiation is incident on the nanowire interconnect, a hotspot forms and can lead to an erroneous output.

Designing superconducting interconnects that mitigate the effect of hotspot formation from ionizing radiation has the potential to dramatically reduce overall error rate in large on-chip superconducting processors.

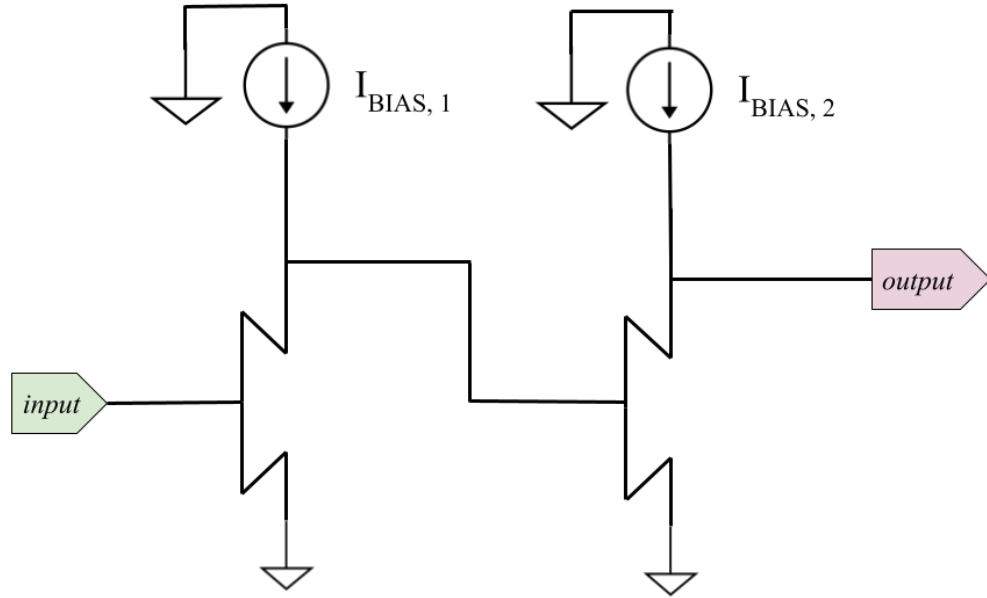


**Figure 4.2.** A cascade of two superconducting nanowire devices. When a current is applied to the input of the left device, a hotspot forms in the device, redirecting its bias current towards the gate of the right device. The current delivered to the gate of the right device then causes a hotspot to form, redirecting the bias current of the second device to the output. If a radiation incident were to occur along the interconnect between the two devices, the current delivered to the second device would be reduced significantly. This could cause unexpected errors, particularly for devices that require a minimum input current to operate.

## 4.2 Generalized Interconnect Model

Here, we present a schematic of the general role of interconnects in a superconducting system: to deliver current from the output of a superconducting device to a load, whether a follow-on superconducting device or a load with non-zero input resistance.

We model a superconducting interconnect as an inductor, where its inductance is determined by the kinetic inductance of the material and the number of squares on-chip. For example, NbN nanometer thin-films have a kinetic inductance of approximately 50 pH/square [61]. To represent a nanowire interconnect of 100 squares, we use an inductance of 5 nH in SPICE simulations. In order to model the effects of incoming ionizing particles in space, we use the SNSPD SPICE model from [62]. Although this model was designed to simulate hotspots from photon absorption, we anticipate ionizing particle interactions to form hotspots in a similar manner [63]. The SNSPD model in SPICE allows us to simulate the dynamics within an interconnect as superconductivity is broken and healed. For the interconnect, we chose a critical

current of  $52.5 \mu\text{A}$ . In order to operate below the critical current, we create a bias current of  $47 \mu\text{A}$ . In these SPICE simulations, we use a voltage-controlled switch to model superconducting devices. The low resistance of the switch is  $1 \mu\Omega$ , to model a device in the superconducting state. The high resistance of the switch is  $2 \text{ k}\Omega$ , to model a device with a resistive channel. Figure 4.3 shows the generalized superconducting interconnect model. Figure 4.4 shows the SPICE equivalent circuit for simulation.

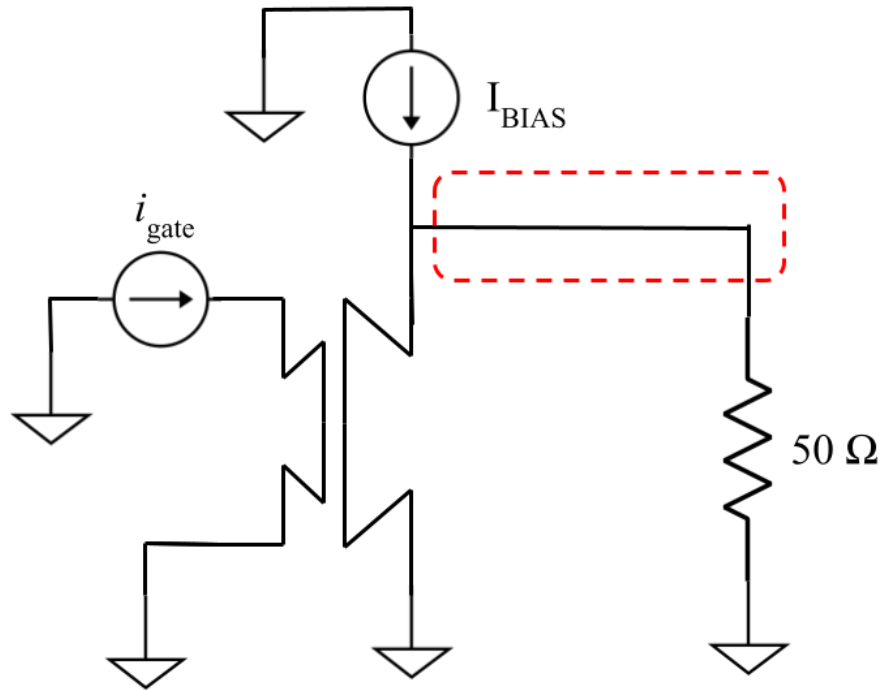


**Figure 4.3.** A general model for simulation of radiation effects along superconducting interconnects. The interconnect, boxed in dotted red, connects the output of a superconducting device to a resistive load. A DC bias current feeds the superconducting device, which is triggered by a current on the gate. This superconducting device operates by thermally switching the channel, which is explained more in Chapter 5.

Using the SPICE schematic shown in Figure 4.4, we can simulate the effects of radiation incidents along superconducting interconnects for both DC and AC scenarios. In both cases, we see an unexpected disturbance in the current being delivered to the load, which is a  $50 \Omega$  resistor in this simulation.

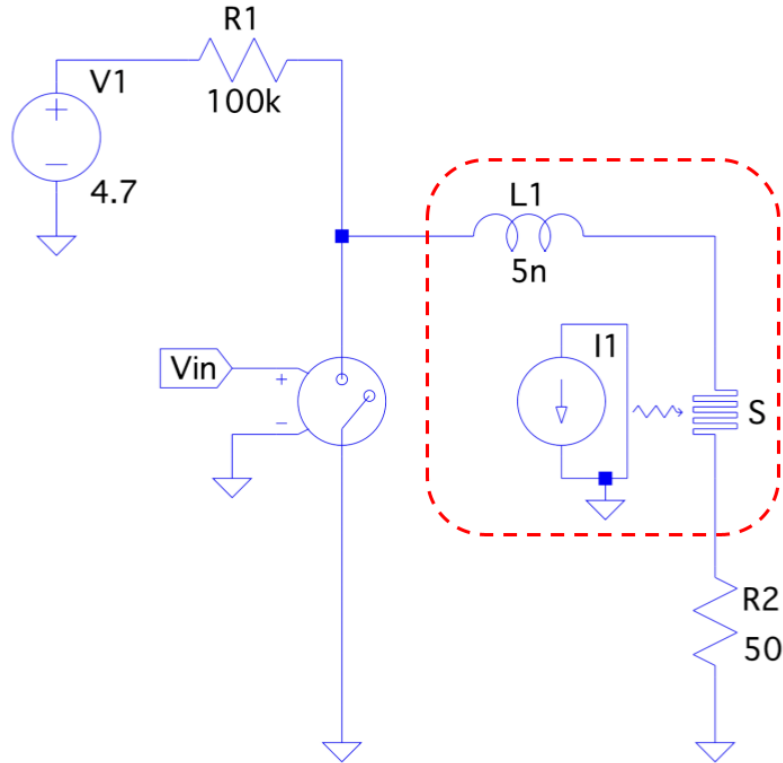


**Figure 4.4.** A SPICE model for simulating the effects of ionizing radiation along superconducting interconnects. The exposed interconnect in this schematic is enclosed by a dotted red box. It includes an inductor, to model the kinetic inductance of a nanowire, and a SNSPD, to model hotspot formation from particle interaction. A superconducting device is modeled using a voltage-controlled switch. Bias current is supplied using a 4.7 V DC voltage source and a 100 k $\Omega$  resistor.

In the AC scenario, we drive the superconducting device with a 25 MHz square wave. In a circuit without errors, we anticipate the bias current in the superconducting device to be redirected to the load with a near-identical waveform as the driving signal, only differentiated by the charge and discharge time of the inductance in the nanowire interconnect. This proper operation is shown in Figure 4.5, where no photon events were simulated on the SNSPD. Next, we simulated photon incidents on the interconnect region to represent hotspots from ionizing radiation. The output signal plot in the presence of radiation is shown in Figure 4.6. With radiation events along the superconducting interconnect, we see the current delivered to the load drop dramatically, due to the current divider that forms between the hotspot resistance in the superconducting device and the hotspot resistance in the interconnect.

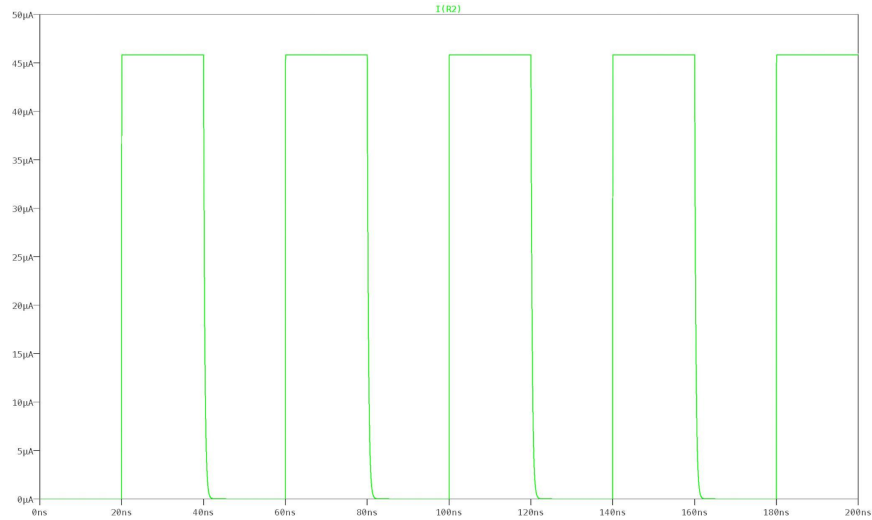


**Figure 4.5.** A SPICE simulation of the current through the load resistor (green), R2, from the schematic shown in Figure 4.4. The voltage-controlled switch is operated at a frequency of 25 MHz, with a 50% duty cycle square wave. In this plot, where no photon incidents occur, the output current has a near-identical waveform as the square wave input. The discharge delay from the inductance of the superconducting interconnect is visible at the falling edge of the pulses. This circuit properly delivers current to a load.

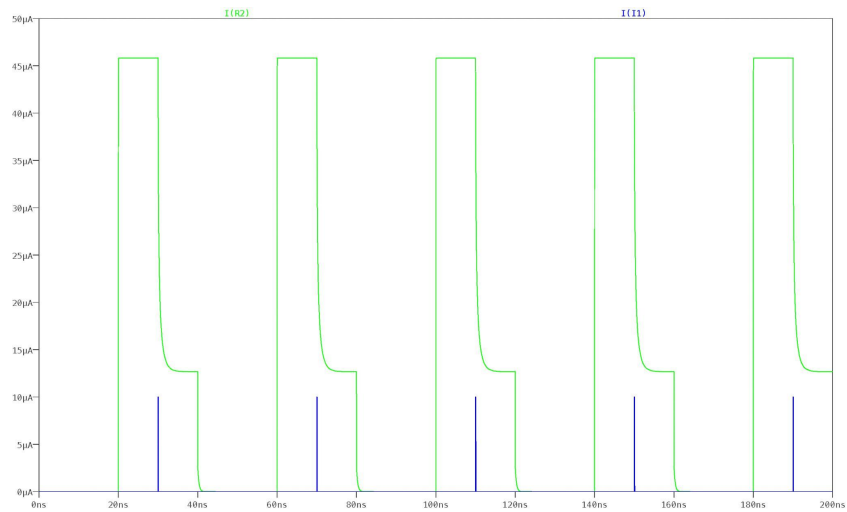


**Figure 4.6.** A SPICE simulation of the current through the load resistor (green), R2, from the schematic shown in Figure 4.4. The voltage-controlled switch is operated at a frequency of 25 MHz, with a 50% duty cycle square wave. In this plot, we trigger hotspots in the SNSPD embedded within the interconnect. These events are marked by the blue pulses, indicating the current applied to the SNSPD model to trigger hotspot formation. Once a hotspot forms along the interconnect, voltage delivered to the load resistor drops significantly because of the current divider that forms between the resistance of the superconducting device (represented by the voltage-controlled switch) and the hotspot resistance along the interconnect. The hotspot along the interconnect heals once current can return to the superconducting device.

In the DC scenario, we drive a superconducting device with a constant input, intended to continuously redirect the bias current through the interconnect to a load. This is shown in Figure 4.7, with no radiation present. Next, we simulate photon incidents along the interconnect and again see a dramatic drop in current delivered to the load. This is shown in Figure 4.8. In the DC scenario, the error is not transient. This is because the interconnect enters a latched state, where the only way to restore superconductivity is to reduce the current below the retrapping current of the nanowire. Without methods of error detection, this will only occur when the gate signal to the superconducting device is turned off.

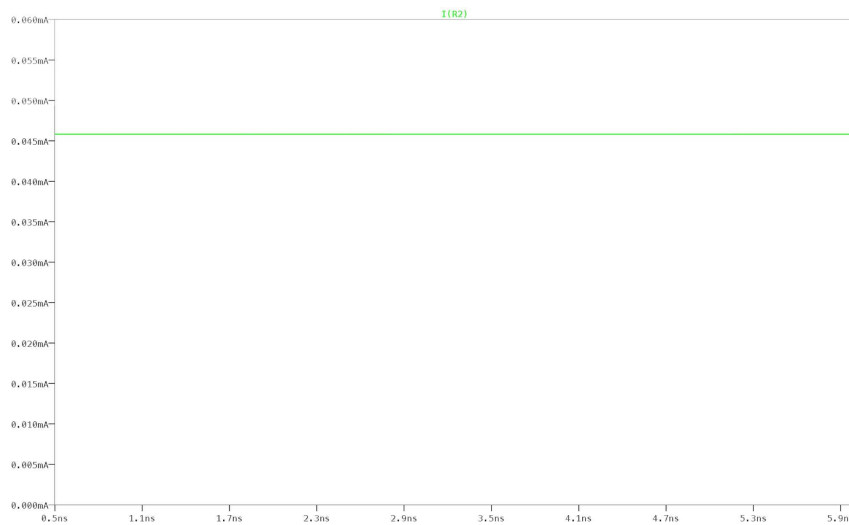


**Figure 4.7.** A SPICE simulation of the current through the load resistor (green), R2, from the schematic shown in Figure 4.4. In this scenario, a constant gate signal is applied to the superconducting device (represented by the voltage-controlled switch). With the device constantly in a normal state, nearly all of the 47  $\mu\text{A}$  bias current redirects to the load resistor, as expected. No radiation incidents are simulated in this plot.

These two scenarios demonstrate how hotspots formed by ionizing radiation will cause errors in superconducting logic for both AC and DC signals. In order to operate a superconducting nanowire-based processor on a Starshot probe, where radiation shielding is not feasible due to mass and size constraints, we must design resiliency against these errors from radiation in another manner.

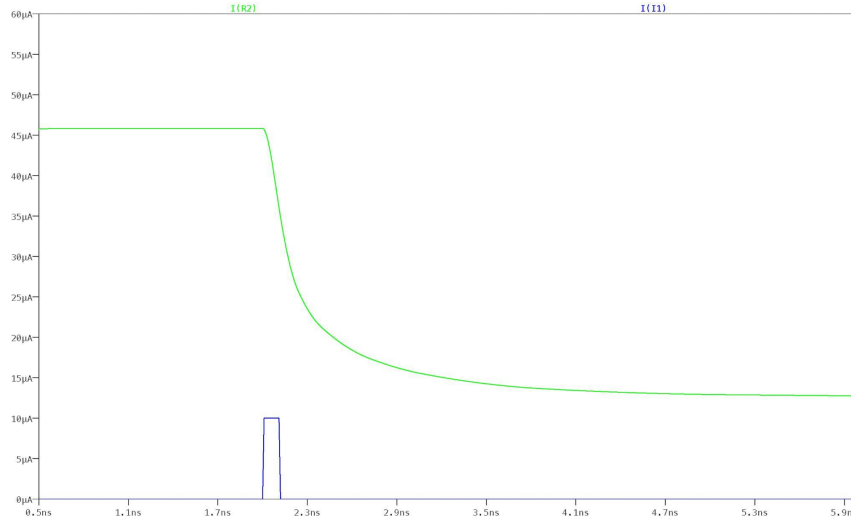


**Figure 4.8.** A SPICE simulation of the current through the load resistor (green), R2, from the schematic shown in Figure 4.4. In this scenario, a constant signal is applied to the superconducting device (represented by the voltage-controlled switch). Now, we also simulate a radiation incident along the interconnect using the SNSPD model. This incident is shown in blue on the plot. Prior to the incident radiation, the current delivered to the load is  $47 \mu\text{A}$ , as expected. Once a hotspot forms along the interconnect due to the SNSPD triggering, current delivered to the load drops dramatically, approaching a steady-state value. This final current value is determined by the ratio of the hotspot resistance along the interconnect to the resistance in the superconducting device. The hotspot along the interconnect will only heal when current can redirect back into the superconducting device.

### 4.3 Shunted Interconnect Design

To resolve the issues illustrated in the previous section, where collisions between ionizing space radiation and superconducting interconnects cause dramatic fluctuations in current through a circuit, we propose a shunted interconnect design.

In this design, a low resistance shunt is placed in parallel with any exposed interconnects. By doing so, the resistance of any hotspot that forms along the interconnect is roughly limited to the value of the shunt resistor. The current traveling through a superconducting interconnect can temporarily redirect through this low resistance shunt if a hotspot does form due to radiation, but it can quickly return to the interconnect once the hotspot heals and superconductivity is restored.

We originally investigated a parallel superconducting nanowire approach, where an interconnect would consist of multiple discrete nanowires run in parallel, but decided against this. We did so because magnetic flux would become trapped in the superconducting loops formed by the parallel lines as hotspots formed and healed.

Figure 4.9 shows a SPICE circuit schematic using the shunted interconnect design. The added shunt is placed in parallel with the region of the interconnect where radiation incidents are simulated using the SNSPD model. The shunt restores expected interconnect operation for both the AC and DC scenarios, which were shown in Figures 4.5 and 4.7, respectively. Figure 4.10 shows a plot of the current through the load in the AC scenario, where radiation is simulated in the shunted configuration. Figure 4.11 shows a plot of the current through the load in the DC scenario, where radiation is simulated in the shunted configuration. In both cases, a slight disturbance can be seen at the moment the SNSPD is triggered, representing an incident with ionizing radiation, however the overall stability of the system is restored.

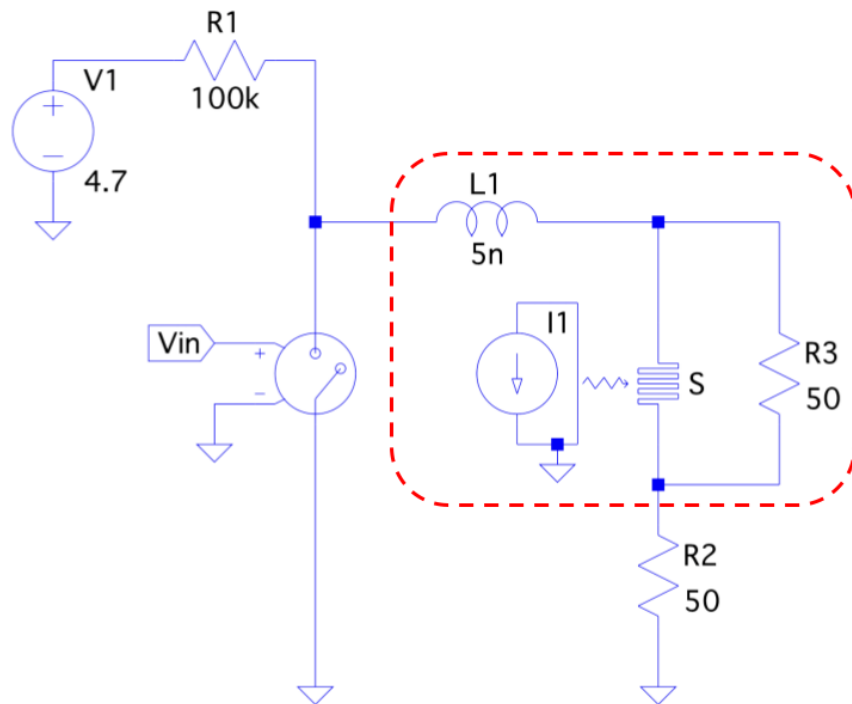


**Figure 4.9.** A SPICE schematic for simulating the effects of ionizing radiation along superconducting interconnects, now with a  $50\ \Omega$  shunt resistor added. The exposed interconnect in this schematic is enclosed by a dotted red box. Adding the shunt resistor restores expected operation even in the presence of radiation along the exposed interconnect.

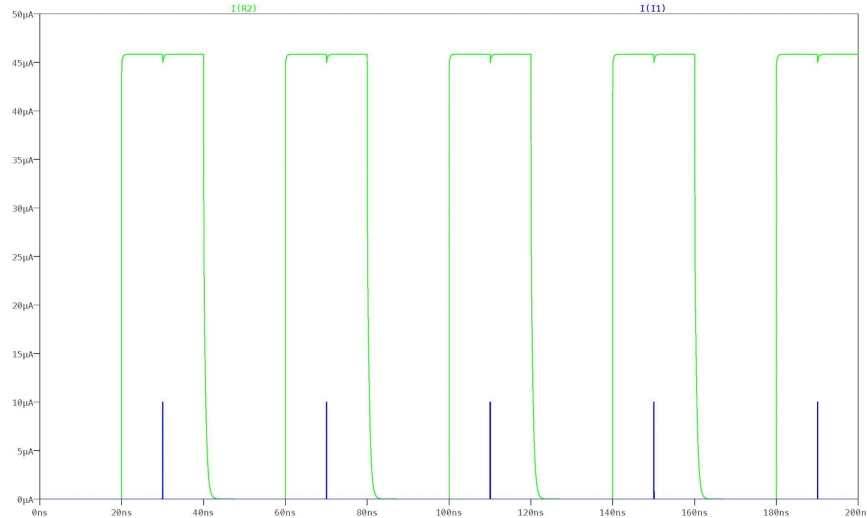


**Figure 4.10.** A SPICE simulation of the current through the load resistor (green), R2, from the schematic shown in Figure 4.9. The voltage-controlled switch is operated at a frequency of 25 MHz, with a 50% duty cycle square wave. In this plot, radiation incidents are simulated along the interconnect at the time of the blue pulses. At the time of the radiation incidents, a minor disturbance is seen in the current delivered to the load. This is due to the temporary redirection of current within the interconnect to the shunt resistor. Once the hotspot from radiation heals, the current returns to the interconnect.

A suitable alternative for the shunted interconnect design would be to replace all superconducting interconnects with a very low resistance wire, on the order of  $1 \Omega$ . By doing so, no shunt would be needed because the hotspot creation mechanism is unique to wires in a superconducting state. Without any superconducting interconnects, this issue of highly resistive regions connecting components would not occur. However, practical implementation of resistive interconnects would be difficult for two reasons. First, current on-chip resistor fabrication technology using Ti-Au films has a resistance near  $5 \Omega/\text{square}$  [64]. For long interconnects, the total resistance along a line would be much too large to use with superconducting devices. Secondly, we do not understand the impact that radiation could have on the resistive materials. Although a hotspot will not form, there may still be undesired effects that could cause disturbances in the electronics. Future research should consider low-resistance interconnects for superconducting devices in high radiation environments.

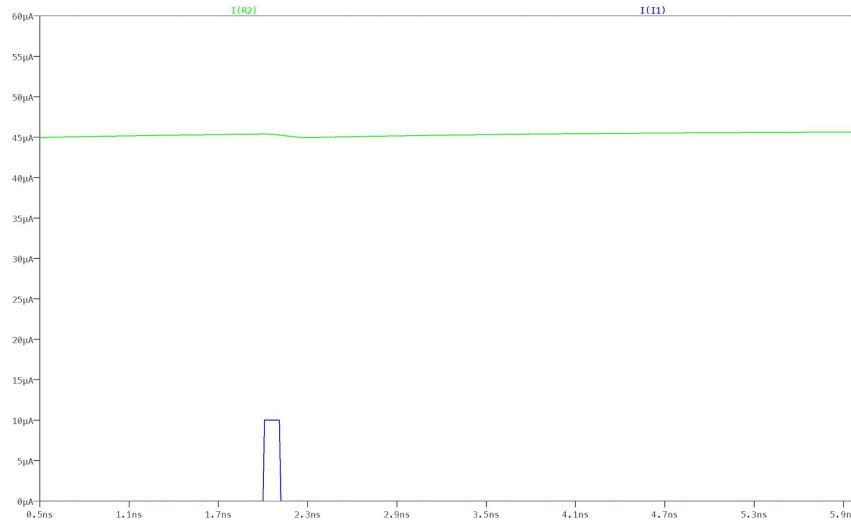


**Figure 4.11.** A SPICE simulation of the current through the load resistor (green), R2, from the schematic shown in Figure 4.9. In this scenario, a constant signal is applied to the superconducting device (represented by the voltage-controlled switch). We also simulate a radiation incident along the interconnect (blue). At the moment the hotspot forms in the interconnect, we see a small drop in the current delivered to the load, due to the added resistance of the 50  $\Omega$  shunt that current redirects through. Once the hotspot heals in the interconnect, we see the current delivered to the load restore to its original value.

In SPICE simulations, the shunted interconnect design shows promising signs of preventing drastic errors in superconducting circuits due to impacts with ionizing radiation. This simple method of designing resilience may enable the operation of superconducting microprocessors in high radiation environments.

## 5 Fabrication and Testing of Superconducting Electronics

The final focus of this research was the fabrication and testing of superconducting nanowire devices relevant to the Starshot project. In this chapter, we present the layout, fabrication process, and early results from these devices.

### 5.1 Layout of Devices

The fabrication consisted of 24 devices on a 1 cm<sup>2</sup> chip. These devices consisted of a variety of nanowire devices: single constrictions, SNSPDs, single-layer planar hTrons (“phTrons”), shunted and non-shunted interconnect patterns, and micrometer-scale nTrons. The devices of interest were the phTrons and interconnect patterns with and without shunt resistors.

The intention of this testing was to validate the simulations in Chapter 4, which indicated that resistive shunting of superconducting interconnects adds resilience in the presence of radiation. In order to validate these simulations, we fabricated the superconducting circuit shown in Figure 4.3. This circuit consists of a superconducting switching device, an interconnect, and a 50  $\Omega$  load. For the switching device, we adapted the existing hTron model into a planar device, entirely fabricated on a single layer of NbN [13]. This heat-based device was chosen over the more traditional nTron device because it avoids current from the gate leaking into the channel and possibly to the output [12]. In order to fabricate a superconducting interconnect and expose it to radiation capable of hotspot formation, we employed a SNSPD. By operating the device while exposed to a high powered laser (wavelength of 405 nm), we created a suitable radiation environment to cause hotspot formation along the SNSPD interconnect. In our cryogenic testing apparatus, the entire sample was exposed to the laser, so we purposefully designed the dimensions of the non-interconnect nanowires to be large enough such that any absorption of a photon would not be suitable to create a hotspot. The layout of the phTron-SNSPD device is shown in Figure 5.1.

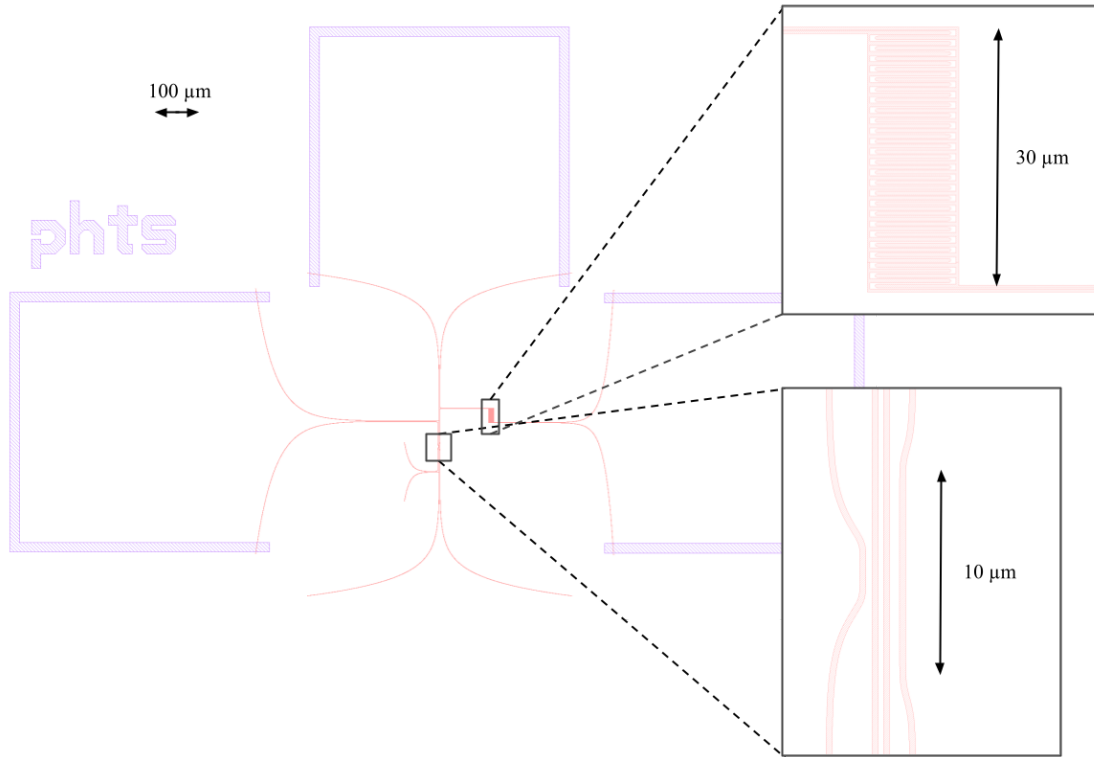


**Figure 5.1.** Layout of the phTron-SNSPD device. This device was used to fabricate the circuit presented in Figure 4.3. This device consists of a planar hTron (phTron), shown in the bottom inset. The phTron has a narrow gate width of 300 nm and a narrow channel width of 500 nm. The drain of the phTron connects to an SNSPD, shown in the upper inset. The width of the SNSPD wires is 150 nm. The SNSPD has an area of 2000 squares. The three pads, shown in purple, are used to connect to various off-chip electronics, discussed more below. The 50  $\Omega$  load and 50  $\Omega$  shunt were soldered onto a PCB then wirebonded to the sample.

Multiple isolated phTrons were also included on-chip. Figure 5.2 shows the layout of these isolated devices, which have identical dimensions to the phTron-SNSPD devices, but no SNSPD on their output. As a standalone device, the principle of the phTron is identical to that of the nTron and hTron: application of a signal at the gate can cause a region in the channel to switch out of the superconducting state [12, 13]. Whereas the nTron accomplishes this switching of the channel by directly injecting current at the gate, and the hTron accomplishes this switching by using a heater directly above the channel, the phTron was intended to perform switching by laterally heating the channel [12, 13]. Since the phTron is fabricated entirely of NbN, which superconducts at the 4.2 K operating temperature of our testing apparatus, there must be enough current in the gate wire to both switch the narrow region into a resistive state *and* dissipate enough heat to suppress superconductivity in the adjacent channel wire.

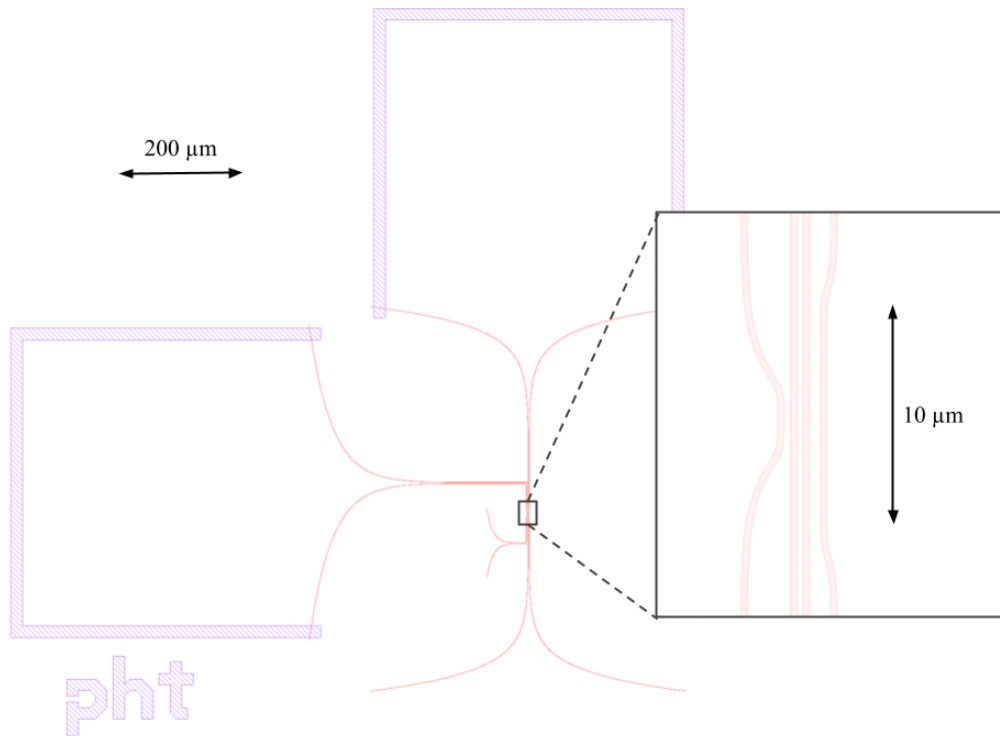


**Figure 5.2.** Layout of the phTron. The region where the narrow sections of the gate and channel are in close proximity is shown in the inset. The gate wire width is  $2\ \mu\text{m}$ , narrowing to  $300\ \text{nm}$  at the region shown in the inset. The channel wire width is  $1\ \mu\text{m}$ , narrowing to  $500\ \text{nm}$  at the region shown in the inset.

## 5.2 Fabrication Methodology

The devices discussed in the previous section were fabricated at MIT in the Quantum Nanostructures and Nanofabrication Laboratory and NanoStructures Laboratory.

Fabrication occurred on a  $1\ \text{cm}^2$  die cut from a Si wafer. The wafer was composed of  $500\ \mu\text{m}$  of silicon substrate capped by  $300\ \text{nm}$  of thermal oxide. A  $7\ \text{nm}$  film of NbN was deposited on top of the oxide layer using an AJA sputtering system. Positive electron-beam resist (ZEP520) was then spun on top of the NbN layer at  $5\ \text{krpm}$  and baked at  $180^\circ\text{C}$ . Patterning of the nanowires was accomplished with electron-beam lithography (Elionix E125). The resist was developed in O-Xylene at  $0^\circ\text{C}$  for 90 seconds then washed in IPA. With the patterned sections of the resist removed, the exposed NbN was then etched using reactive ion etching with  $\text{CF}_4$  at  $50\ \text{W}$ . A single etching process is about a 4 minute cycle that includes 1 minute of etching. This

process was performed 7 times for a cumulative etch time of 7 minutes. After etching, the remaining resist was removed using 1-methyl-2-pyrrolidone (NMP). The sample was placed in NMP, then left in a Symphony Ultrasonic Cleaner with a water bath of 60°C for 2 hours. Once complete, the sample was washed with Acetone and IPA. At this point all fabrication of the sample was complete. Figure 5.3 shows a scanning electron micrograph (SEM) of the phTron-SNSPD after fabrication.

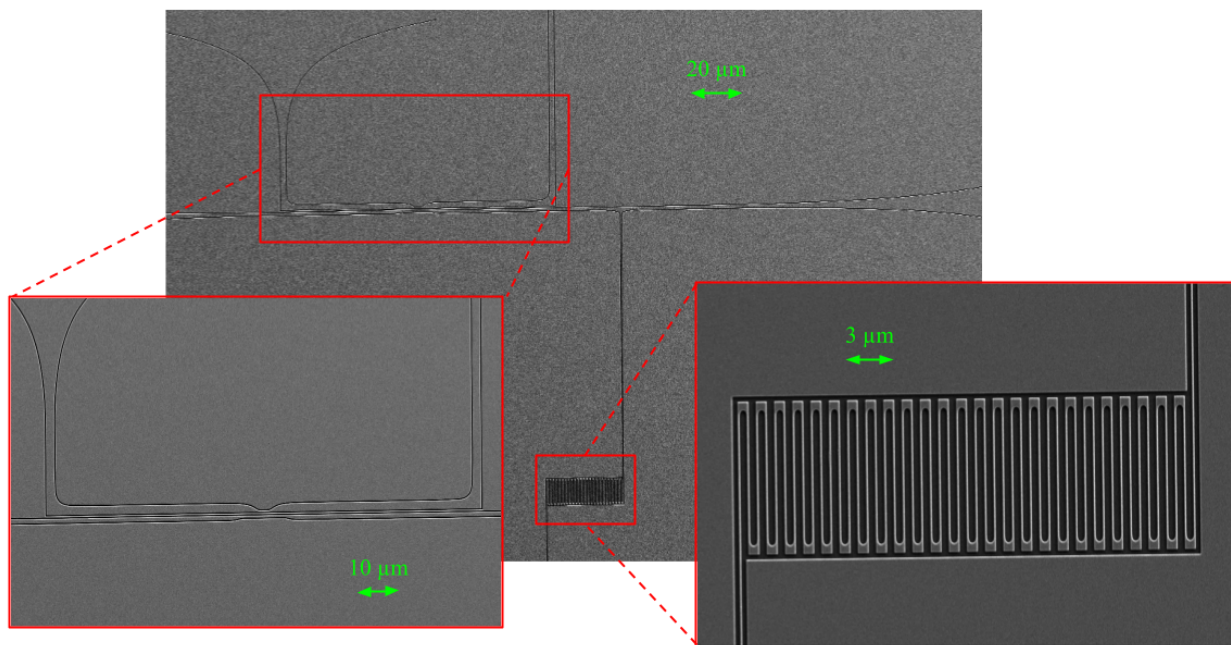


**Figure 5.3.** SEM of the phTron-SNSPD. The channel can be seen in the upper half of the image running horizontally. The inset on the left shows where the narrow regions of the gate and channel meet in the phTron. The inset on the right shows the 150 nm-wide SNSPD meandering connected to the output of the channel.

With a complete sample, we then prepared for cryogenic testing in a specially designed dip probe for use with a helium dewar, discussed more in Section 5.3. First, we prepared the PCB for reading out the proper pins associated with our devices and installed all off-chip resistors. A photograph of the PCB used for testing is shown in Figure 5.4. We then mounted the 1 cm<sup>2</sup> sample on the PCB using GE varnish, which was then heated at 70°C for 30 minutes to cure. Next, we wirebonded pads on the chip to their respective pins on the PCB for readout. A photograph of the complete PCB and sample is shown in Figure 5.5. At this point, we were ready to mount it in the dip probe and conduct testing.

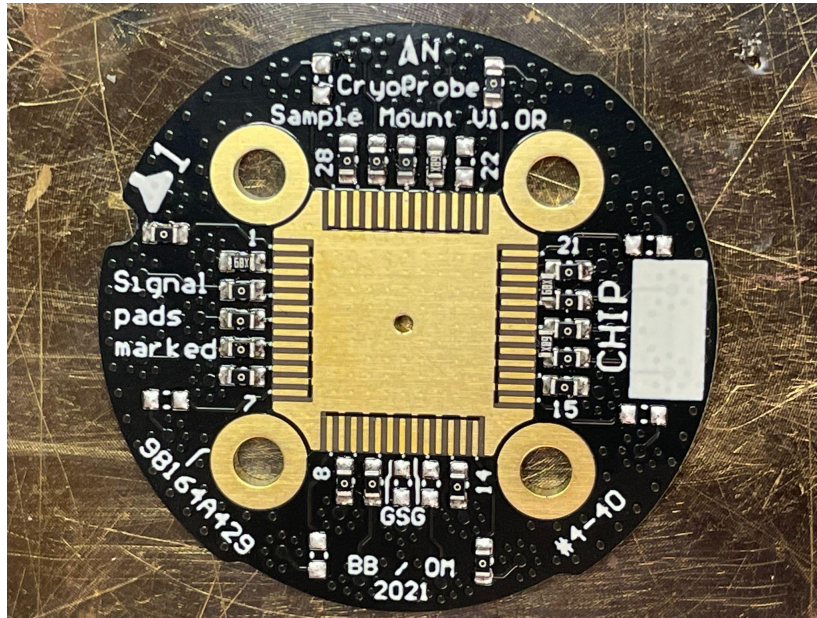


**Figure 5.4.** PCB used in the helium dewar dip probe. A 1 cm<sup>2</sup> area can be seen in the center; this is where the sample will be mounted. Numbered pins are located on the periphery of the chip, beginning with 1 in the top left and incrementing counter clockwise. Each output pin has a spot for an on-chip series resistor. Most pins were shorted to their output, but some have a 50 Ω resistor in series or parallel, such as pins 2 and 20. This PCB was designed by Dr. Brenden Butters and Owen Medeiros.

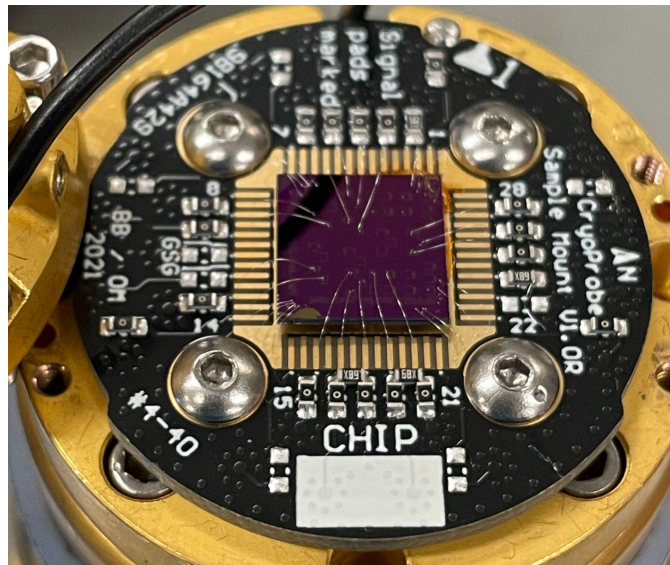


**Figure 5.5.** Complete PCB with mounted and wire-bonded sample. In addition to wirebonds connecting the PCB to each pad being tested, 4 wirebonds from PCB ground to the bulk NbN film are placed in each of the corners.

### 5.3 Early Results

Cryogenic testing of the device occurred in a custom probe designed for rapid testing in a helium dewar, developed by Dr. Brenden Butters [65]. The probe includes 28 RF lines leading from the mounting location on the cold end of the probe to a room temperature manifold, which is shown in Figure 5.6. To operate, the probe is slowly inserted into a helium dewar, cooling the sample down to just above 4 K. A normal cooldown takes 30 minutes.

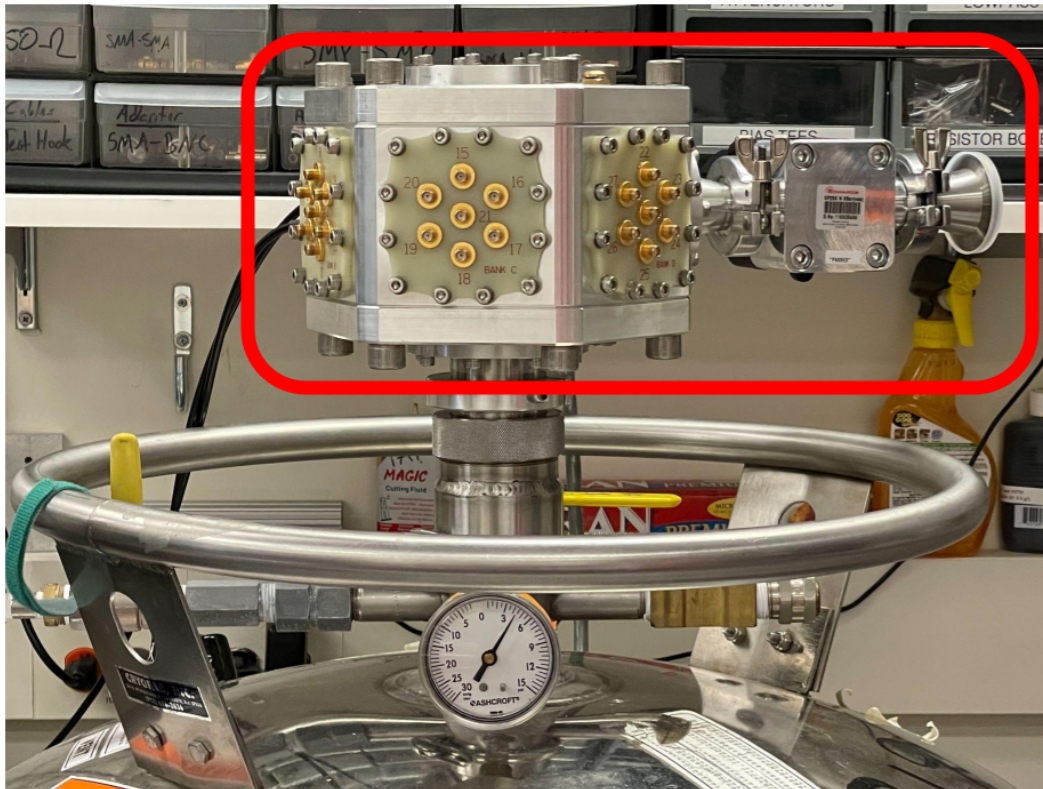


**Figure 5.6.** Helium dip probe fully inserted. The manifold of the dip probe, highlighted in the red box, remains at room temperature for connections to electronics. The probe's shaft is inserted into the dewar, cooling the cap and sample down to 4.2 K.

The initial focus of the testing had been to validate the shunted interconnect design for resilience in radiation environments. However, poor experimental design led to complications in operating the shunted interconnect configuration, which have prevented validation thus far.

These issues were a limited channel current capacity, noise in the testing setup, and poor phTron layout. Operation of the phTron-SNSPD with an AC signal on the gate was unsuccessful because the channel current was limited to the switching current of the SNSPD, due to its width

of 150 nm. While the switching current of the channel was 67  $\mu\text{A}$ , the switching current of the SNSPD was 7  $\mu\text{A}$ . Since the goal was to redirect current through the SNSPD while remaining in a superconducting state (to therefore detect photons), it was important to not create a normal region in the SNSPD by exceeding the switching current of 7  $\mu\text{A}$ . By operating at a small channel current, however, it required an enormous amount of gate current to switch the channel. In testing, we were able to observe a narrow AC operating window (without the laser source turned on) with a channel current of 6  $\mu\text{A}$  and a gate current of 400  $\mu\text{A}$ .

Significant noise in the testing setup was also observed, making AC operation with  $\mu\text{A}$ -scale channel currents unstable. While we dramatically reduced noise in subsequent testing by eliminating a ground loop from the electrical setup, we were unable to finish testing of the phTron-SNSPD.

Lastly, poor design of the phTron may have added thermal latency to the AC operation of the device. This poor design can be seen in the inset of Figure 5.2. Design failures include a large gap between the gate and channel, an unetched NbN line between the gate and channel, and large dimensions overall. The gap between the inner edges of the gate and channel is 865 nm, requiring a large amount of gate current to produce enough heat to affect the channel. In addition to the wide gap, there is an unetched 265 nm-wide NbN wire that runs in the center of the gap. This may cause complications in heat transfer between the gate and the channel and introduce additional mutual inductance.

The large dimensions of the device may also be problematic. The intention of large dimensions was to prevent susceptibility to photon absorptions outside the SNSPD, however it also dramatically increased the current required to create heat within the gate. Although more research may provide specific evidence for the issues in testing of the phTron-SNSPD device, these are some possible problems.

Unable to perform a validation test of the shunted interconnect design, we then shifted to characterizing the discrete phTron devices, which have not been extensively studied [66]. The layout of these devices is shown in Figure 5.2. We completed a DC characterization of two identical phTrons, which we will name phTron A and phTron B. DC characterization of these devices included I-V sweeps of both the gate and channel, as well as an iterative I-V sweep of the channel for numerous gate currents.

The I-V curves of the gate and channel of phTron A are presented in Figure 5.7. We found  $I_{SW,gate} = 35 \mu A$  for the gate and  $I_{SW,channel} = 50 \mu A$  for the channel.

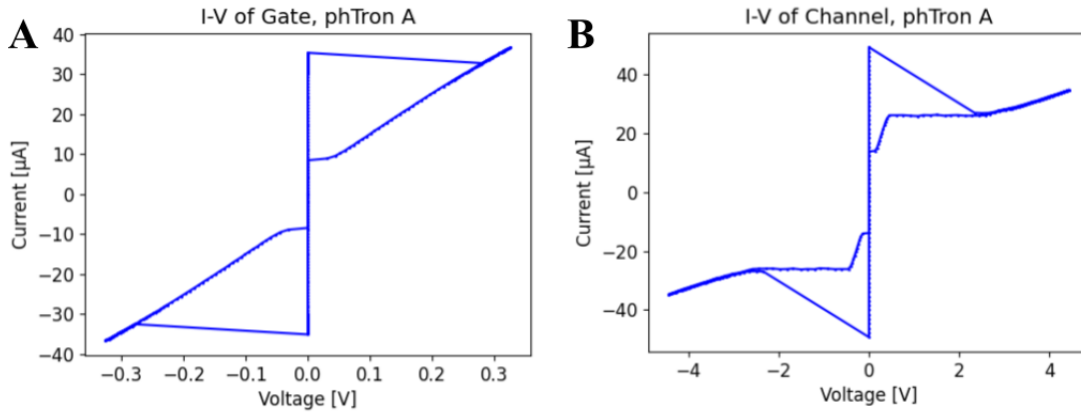


**Figure 5.7.** I-V plots for phTron A. **(A)** I-V of the gate. A switching current of  $35 \mu A$  was measured. **(B)** I-V of the channel. A switching current of  $50 \mu A$  was measured. In these plots, the superconducting region is evident in the center where no voltage develops while the device is below its switching current. Once this switching current is exceeded, the device becomes resistive and resembles an I-V plot of a resistor.

The I-V curves of the gate and channel of phTron B are presented in Figure 5.8. We found  $I_{SW,gate} = 35 \mu A$  for the gate and  $I_{SW,channel} = 63 \mu A$  for the channel.

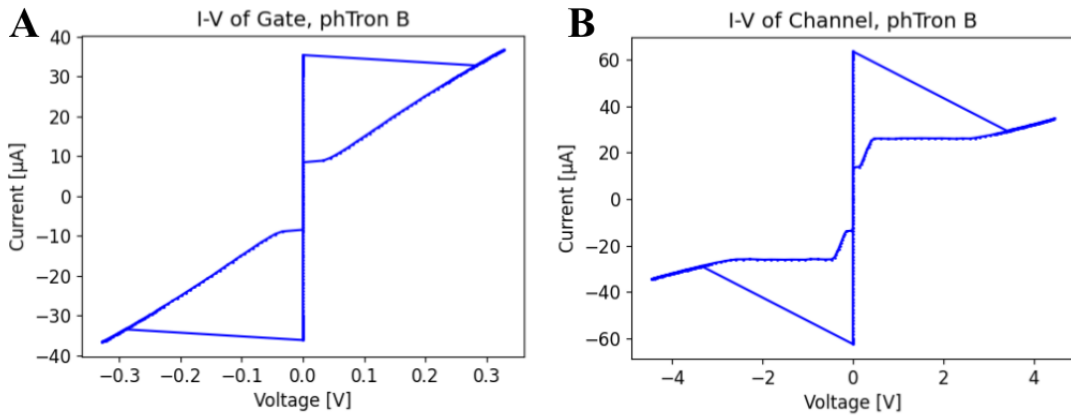


**Figure 5.8.** I-V plots for phTron B. **(A)** I-V of the gate. A switching current of  $35 \mu A$  was measured. **(B)** I-V of the channel. A switching current of  $63 \mu A$  was measured. In these plots, the superconducting region is evident in the center where no voltage develops while the device is below its switching current. Once this switching current is exceeded, the device becomes resistive and resembles an I-V plot of a resistor.

The switching current of the gate of both devices is consistent at 30  $\mu\text{A}$ , however the switching current of the channel of phTron A is 13  $\mu\text{A}$  less than that of phTron B. This was verified in repeated testing, and is likely due to a fabrication defect suppressing superconductivity in the channel. A SEM of phTron A was also taken prior to testing, which could have caused minor damage to the structure via stopping power of the electrons from the microscope beam.

In addition to singular I-V plots, we swept across a wide range of gate currents and measured the I-V of the channel at each gate value. This double sweep measurement is useful for visualizing the boundary between a superconducting and resistive channel region. The double sweep measurements for phTron A are presented in Figure 5.9. The double sweep measurements for phTron B are presented in Figure 5.10. Due to the experimental setup we did not record accurate hotspot resistance values after the switching of the channel; we only know that beyond a certain threshold the channel switched into a normal state. We indicate an entirely superconducting channel as a state of 0 and a resistive channel as a state of 1. Future experiments would benefit from a setup that can accurately measure resistance in the channel after switching occurs, but this may require a very high voltage source depending on the magnitude of the hotspot resistance.

The double sweep plots generally present what we would anticipate. With no gate current, the channel only switches when its critical current is exceeded. For small gate currents (much less than the critical current of the gate), the switching current in the channel is unchanged. Once the current in the gate passes a certain threshold current, the critical current in the channel is suppressed and the channel switches at a current  $I < I_{SW,channel}$ . To be clear, the threshold current of the gate is the current at which we observe suppressed switching in the channel, *not* the critical current of the gate. This distinction is important because we observe the threshold current of the gate to be between 25  $\mu\text{A}$  and 30  $\mu\text{A}$ , which is over 5  $\mu\text{A}$  less than its critical current. This phenomenon is observed in both phTron A and B. This suggests that the gate interferes with the current in the channel even prior to switching itself. Repeated measurements with smaller step sizes on the gate would verify this observation and may lead to a better understanding of its cause.

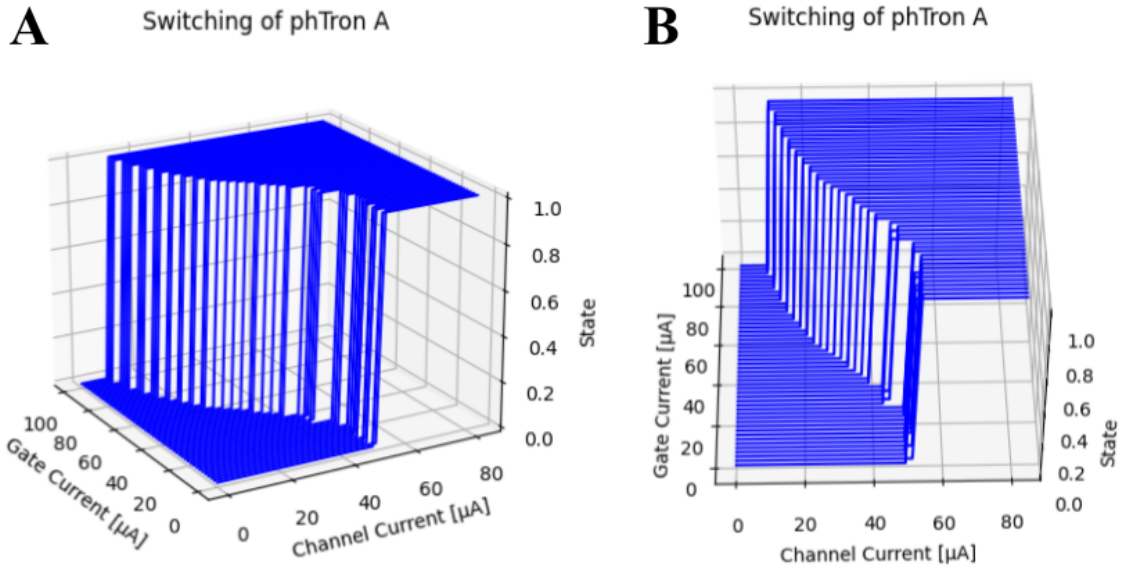


**Figure 5.9.** Gate-channel double sweep plots for phTron A. With no current on the gate, we observe switching in the channel at 50  $\mu\text{A}$ , as expected. Once the current in the gate exceeds 30  $\mu\text{A}$ , we observe suppression of the channel and lower channel currents required to cause switching. (A) and (B) show the same data, just at different plot angles. A state of 0 represents a superconducting channel and a state of 1 represents a switched, resistive channel.

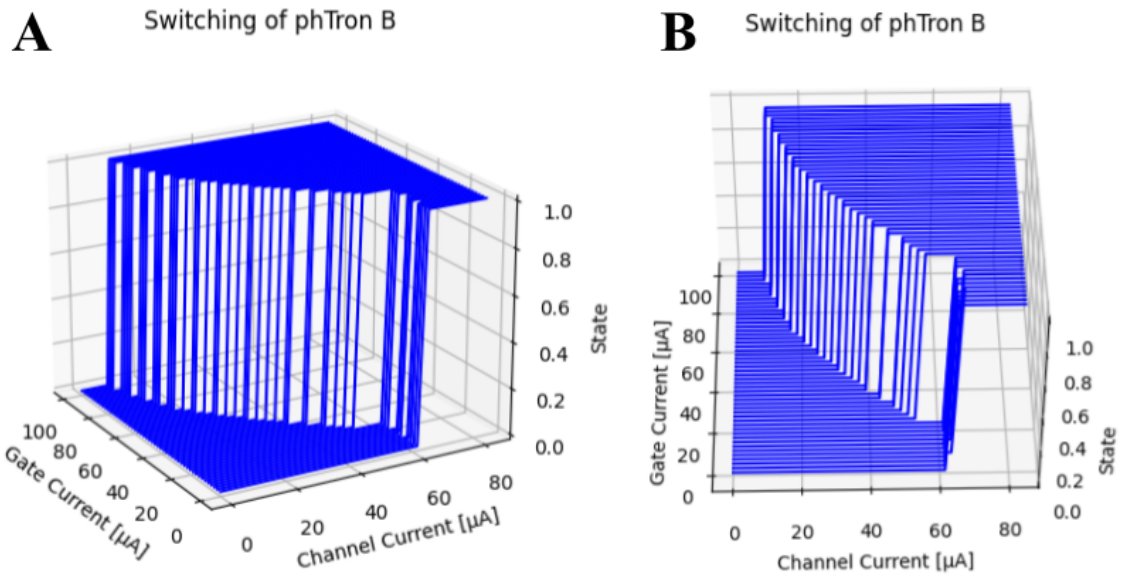


**Figure 5.10.** Gate-channel double sweep plots for phTron B. With no current on the gate, we observe switching in the channel at 63  $\mu\text{A}$ , as expected. Once the current in the gate exceeds 25  $\mu\text{A}$ , we observe suppression of the channel and lower channel current required to cause switching. (A) and (B) show the same data, just at different plot angles. A state of 0 represents a superconducting channel and a state of 1 represents a switched, resistive channel.

An exciting next step for characterization of the phTron devices will be to complete an AC characterization. The intention would be to determine the gray zone between gate pulse height/width and switching probability in the channel for various channel bias currents. A more optimal design should be pursued for high frequency studies. Such a design would reduce the distance between the gate and the channel and remove any superconducting material between the two. A new design should also reduce the overall dimensions of the device, assuming disturbances from environmental radiation are not an issue.

While this testing has not yet validated the benefits of using a shunted interconnect design in the presence of radiation, it did explore a less common superconducting nanowire device, the phTron.

## 6 Conclusions and Future Work

This research highlighted some of the main challenges to employing superconducting nanowire electronics on Starshot probes: radiation and temperature. Although we present a method of mitigating radiation errors in superconducting electronics, more robust resilience will be needed to perform complex on-board processing. The temperature of the spacecraft will determine whether operation of superconducting electronics is possible, and will depend heavily on the chosen transit configuration of the sail. This configuration may be influenced by a variety of factors such as power generation mechanism and on-board transmitter architecture. With these challenges in mind, superconducting electronics remain a promising avenue for sensing and processing capabilities on Breakthrough Starshot probes.

### 6.1 Operability of Onboard Superconducting Electronics

The decision to use superconducting electronics on a Starshot probe must be made by comparing the constraints imposed by the devices with the benefits obtained through their use. Radiation, temperature, and power are primary factors to consider, which we will discuss here. Future investigation into superconducting devices for space applications will benefit not only Starshot, but many other future ventures.

Radiation poses a challenge to superconducting electronics in the form of transient electronic errors. Based on simulations performed that model the interstellar radiation environment, the anticipated transient error rate in superconducting electronics is small. For the face-on sail configuration, we anticipate  $1.8 \times 10^{-7} \frac{\text{errors}}{10 \text{ ns} \cdot \mu\text{m}^2}$ . For the side-on sail configuration, we anticipate only  $1.23 \times 10^{-17} \frac{\text{errors}}{10 \text{ ns} \cdot \mu\text{m}^2}$ . Coupled with redundant logic and the resilient interconnect design presented in Chapter 4, it appears that single errors from radiation may be manageable. The effects of the total radiation dose on the superconducting materials are not yet well understood.

Since superconductors only exhibit their unique properties when they are below a critical temperature, the temperature of the sail is important for determining whether they can operate onboard. No matter the sail configuration, heating is likely to occur on the front surface due to

collisions with interstellar gas. Preliminary estimates from [41] suggest ambient sailcraft temperature upwards of 100 K. However, these calculations assumed a strictly face-on configuration. By adopting a side-on sail configuration, the sail would minimize its cross section to interstellar gas and dust, and maximize its surface area for radiative cooling. In this configuration, we estimate an equilibrium spacecraft temperature of 3.28 K (from Chapter 3). By operating electronics at such a low temperature, we may even be able to create a drastic thermal gradient across the sail, allowing for passive thermoelectric power harvesting from the Seebeck Effect [67].

The power factor for superconducting nanowire electronics is appealing. With switching energies over 100x smaller than in 7 nm CMOS, superconducting processing elements may be suited for Starshot, where the power budget may be incredibly low. However, more research is needed to assess total power consumption in a scaled superconducting processor. Only then could an accurate assessment be made in the context of this mission.

## **6.2 Superconducting Electronics in Starshot Ground Station**

Independent of their use onboard Starshot probes, superconducting nanowire electronics have a very strong case for use in the ground receiver station for Starshot downlink communications. Superconducting nanowire single photon detectors (SNSPDs) may be needed to perform the direct detection and precise time-tagging of photons for the proposed pulse position modulation downlink scheme [33]. Such a scheme requires extremely high detection efficiency and ultra-low dark count rates. Sub-optimal performance in either of these categories drastically reduces the data rate [33].

The use of SNSPDs for ground reception of optical communications from space was demonstrated in the Lunar Laser Communication Demonstration [68]. This proof-of-concept showed that SNSPDs have the receiver capabilities required for long range optical communications into space.

There is, however, a major cost associated with operating SNSPDs: cooling power. In order to operate at cryogenic temperatures for detection, superconducting detectors must be maintained below their critical temperature. To use SNSPDs in the 1 km<sup>2</sup> ground receiver station for Starshot will require not only intellectual, but also financial investment. There are

continuous, gradual research advancements in the operating temperature of high-quality SNSPDs, which may help lower cooling costs. In 2021, a 20 K SNSPD fabricated with  $\text{MgB}_2$  was demonstrated to have high performance metrics [69].

### 6.3 Future Work

There are many avenues for further research of superconducting nanowire electronics that are relevant for the Breakthrough Starshot project.

Principally, emphasis should be placed on scaling the number of superconducting nanowire devices on-chip and demonstrating more complex logical operations. Research should also seek to improve and integrate superconducting memory arrays with logic elements [13]. By gradually increasing the scale and functionality of on-chip superconducting processors, we may make them more feasible for Starshot missions and similar space applications.

In continuation of the research in this thesis, neutron irradiations of superconducting materials will be completed at the MIT Nuclear Reactor test facility. These tests intend to simulate a total radiation dose that would occur on the electronics in space. We intend to observe the effect of the total radiation dose on the superconducting properties of the thin-film superconductors to get a sense of how space radiation may impact operation. We are pursuing testing of  $\text{NbN}$ ,  $\text{MoSi}_2$ , and  $\text{WSi}_2$  nanofilms. To our knowledge, nanofilms of these materials have not been radiated with the purpose of observing changes in superconducting properties.

Tangential applications of superconducting nanowire devices should also be heavily explored for Starshot, not only processing elements. For example, high efficiency SNSPDs with higher critical temperatures may be a critical component in the ground receiver array. Superconducting elements can also be explored for onboard sensors, such as magnetic field sensors [70].

With so many innovations remaining in the field of superconducting nanowires, I'm excited to see where the field advances next.

## Bibliography

- [1] G. Popkin, "What it would take to reach the stars," *Nature*, vol. 542, pp. 20-22, 2017.
- [2] A. Stillmaker and B. Baas, "Scaling equations for the accurate prediction of CMOS device performance from 180 nm to 7 nm," *Integration*, vol. 58, pp. 74-81, 2017.
- [3] "The artemis plan: NASA's lunar exploration program overview," *NASA*, 2020.
- [4] "NASA's Europa clipper," *NASA*, <https://europa.nasa.gov>. Accessed 21 April 2022.
- [5] S. Frazier, "Deep space optical communications," *NASA*, [https://www.nasa.gov/mission\\_pages/tm/dsoc/index.html](https://www.nasa.gov/mission_pages/tm/dsoc/index.html). Accessed 21 April 2022.
- [6] R. Frisbee, "Advanced space propulsion for the 21st century," *Journal of Propulsion and Power*, vol. 19, no. 6, pp. 1129-1135, 2003.
- [7] "The sunshield Webb," *NASA*, <https://webb.nasa.gov/content/observatory/sunshield.html>. Accessed 16 April 2022.
- [8] C. Leonard, "Challenges for electronic circuits in space applications," *Analog Devices*, <https://www.analog.com/media/en/technical-documentation/tech-articles/thought-leadership/challenges-for-electronic-circuits-in-space-applications.pdf>. Accessed 27 April 2022.
- [9] M. Knopp, et al., "Towards the utilization of optical ground-to-space links for low earth orbiting spacecraft," *IAF*, 2018.
- [10] S. Bayard, et al., "Vision-based navigation for the NASA mars helicopter," *AIAA SciTech*, 2019.
- [11] J. Yang, et al., "Fabrication development for nanowire GHz-counting-rate single-photon detectors," *IEEE Applied Superconductivity*, vol. 15, no. 2, pp. 626-630, 2005.
- [12] A. McCaughan and K. Berggren, "A superconducting-nanowire three-terminal electrothermal device," *Nano Letters*, vol. 14, no. 10, pp. 5748-5753, 2014.
- [13] B. A. Butters, R. Baghdadi, M. Onen, E. A. Toomey, O. Medeiros, and K. Berggren, "A scalable superconducting nanowire memory cell and preliminary array test," *Superconductor Science and Technology*, vol. 34, no. 3, 2021.
- [14] "Radar for Europa assessment and sounding," *JPL*, [https://www.lpi.usra.edu/opag/meetings/aug2015/presentations/day-1/8\\_f\\_REASON.pdf](https://www.lpi.usra.edu/opag/meetings/aug2015/presentations/day-1/8_f_REASON.pdf). Accessed 16 April 2022.

- [15] “NASA’s Europa clipper instruments,” NASA, <https://europa.nasa.gov/spacecraft/instruments>. Accessed 21 April 2022.
- [16] P. Lubin, “A roadmap to interstellar flight,” *Journal of the British Interplanetary Society*, vol. 69, pp. 40-72, 2016.
- [17] S. Weinreb, “Low cost microwave ground terminals for space communications,” *JPL*, 2003.
- [18] “Thermal control,” NASA, <https://www.nasa.gov/smallsat-institute/sst-soa/thermal-control>. Accessed 26 March 2022.
- [19] J. Dickman, “Low-temperature spacecraft: challenges and opportunities,” *Forum on Innovative Approaches to Outer Planetary Exploration*, pp. 25, 2001.
- [20] E. G. Stassinopoulos, “The earth’s trapped and transient space radiation environment,” *NATO ASI Series*, vol. 154, pp. 5-36. 1988.
- [21] M. A. Xapsos, “Technology readiness overview: CMOS ultra-low power radiation tolerant integrated circuits,” *NASA*.
- [22] “Did bad memory chips down Russia’s Mars probe?,” *IEEE Spectrum*, <https://spectrum.ieee.org/did-bad-memory-chips-down-russias-mars-probe>. Accessed 13 April 2022.
- [23] “Power,” NASA, <https://www.nasa.gov/smallsat-institute/sst-soa/power/>. Accessed 26 March 2022.
- [24] “Radioisotope thermoelectric generators,” NASA-JPL, <https://voyager.jpl.nasa.gov/mission/spacecraft/instruments/rtg/>. Accessed 07 April 2022.
- [25] K. Hass and H. Shaw, “Cryogenic operation of ultra low power CMOS,” *9th NASA Symposium on VLSI Design*, pp. 1-3, 2000.
- [26] P. Gregshammer and H. W. Weber, “The effects of high fluence neutron irradiation on the superconducting properties of magnetron sputtered NbN films,” *Journal of Applied Physics*, vol. 64, no. 3, pp. 1301-1306, 1988.
- [27] H. Shibata, “Superconducting single-photon detectors,” *NTT Technical Review*, vol. 9, no. 9, 2011.
- [28] G. Anglada-Escudé, et al., “A terrestrial planet candidate in a temperate orbit around Proxima Centauri,” *Nature*, vol. 536, pp. 437-440, 2016.

- [29] S. Worden, “Progress on the Starshot laser propulsion system,” *Applied Optics*, vol. 60, no. 31, pp. 20-23, 2021.
- [30] H. Atwater, et al., “Materials challenges for the Starshot lightsail,” *Nature Materials*, vol. 17, pp. 861-867, 2018.
- [31] M. Taghavi, M. Salary, and H. Mosallaei, “Multifunctional metasails for self-stabilized beam-riding and optical communication,” *Nanoscale Advances*, vol. 7, 2022.
- [32] D. Messerschmitt, P. Lubin, and I. Morrison, “Technological challenges in low-mass interstellar probe communication,” *Journal of the British Interplanetary Society*, vol. 73, no. 12, pp. 438-445, 2020.
- [33] D. Messerschmitt, P. Lubin, and I. Morrison, “Challenges in Scientific Data Communication from Low-mass Interstellar Probes,” *The American Astronomical Society*, vol. 249, no. 36, 2020.
- [34] N. English, “Space telescopes: capturing the rays of the electromagnetic spectrum,” *Springer*, 2017.
- [35] J. D. Slavin and C. Frisch, “The boundary conditions of the heliosphere: photoionization models constrained by interstellar and in situ data,” *Astron. Astrophys.*, vol. 491, pp. 53-68, 2008.
- [36] J. Amos, “Neighbouring star Proxima Centauri has Earth-sized planet,” BBC News, <https://www.bbc.com/news/science-environment-37167390>. Accessed 28 April 2022.
- [37] E. G. Stassinopoulos and K. A. LaBel, “The near-earth space radiation environment for electronics,” *Proc. IEEE*, vol. 76, no. 11, 1988.
- [38] J. Lockwood, “Neutron measurements in space,” *Space Science Reviews*, vol. 14, no. 5, pp. 663-719, 1972.
- [39] J. A. Simpson, “Elemental and isotopic composition of the galactic cosmic rays,” *Ann. Rev. Nucl. Part. Sci.*, vol. 33, pp. 323-381. 1983.
- [40] R. London and J. Early, “Evaluation of the hazard of dust impacts on interstellar spacecraft,” *Journal of the British Interplanetary Society*, 2018.
- [41] T. Hoang, A. Lazarian, B. Burkhart, and A. Loeb, “The interaction of relativistic spacecrafts with the interstellar medium,” *The Astrophysical Journal*, vol. 837, no. 5, 2017.
- [42] “Relativistic energy,” *Libre Texts*, vol. Physics, no. 5.10, 2022.

- [43] “Ionizing radiation,” Occupational Safety and Health Administration, <https://www.osha.gov/ionizing-radiation/background>. Accessed 14 March 2022.
- [44] N. Bohr, “On the theory of the decrease of velocity of moving electrified particles on passing through matter,” *The London, Edinburgh, and Dublin Philosophical Magazine and Journal of Science*, vol. 25, no. 145, pp. 10-31, 1913.
- [45] W. Lotz, “Electron binding energies in free atoms,” *J. Opt. Soc. Am.*, vol. 60, pp. 206-210, 1970.
- [46] K. Nordlund, “Energy loss of energetic ions,” <http://beam.helsinki.fi/~knordlun/mdh/rangetext.html>. Accessed 05 December 2021.
- [47] C. Amsler, H. Bichsel, D. Groom, and S. Klein, “Passage of particles through matter,” *Review of Particle Physics*, pp. 267-280, 2008.
- [48] J. Ziegler, “The stopping and range in compounds,” SRIM, <http://www.srim.org/SRIM/Compounds.htm>. Accessed 19 October 2021.
- [49] B. Srivastava and S. Mukherji, “Range and stopping-power equations for heavy ions,” *Physical Review A*, vol. 14, no. 2, pp. 718-725, 1976.
- [50] H. Bethe, “Theory of the passage of fast corpuscular rays through matter,” *Annalen der Phys.*, vol. 397, pp. 325-400, 1930.
- [51] R. M. Sternheimer, M. J. Berger, and S. M. Seltzer, “Density effect for the ionization loss of charged particles in various substances,” *Atomic Data and Nuclear Data Tables*, vol. 30, pp. 261-271, 1984.
- [52] D. I. Thwaites, “Bragg’s rule of stopping power additivity: a compilation and summary of results,” *Radiation Research*, vol. 95, pp. 495-518, 1983.
- [53] W. H. Bragg and R. Kleeman, “On the alpha-particles of radium, and their loss of range in passing through various atoms and molecules,” *The London, Edinburgh, and Dublin Philosophical Magazine and Journal of Science*, vol. 10, no. 57, pp. 318-340, 1905.
- [54] L. You, “Superconducting nanowire single-photon detectors for quantum information,” *Nanophotonics*, vol. 9, no. 9, pp. 2673-2692, 2021.
- [55] W. Zhang, et al., “NbN superconducting nanowire single photon detector with efficiency over 90% at 1550 nm wavelength operational at compact cryocooler temperature,” *Science China Physics, Mechanics & Astronomy*, vol. 60, no. 12, pp. 1-10, 2017.

- [56] C. Natarajan, M. Tanner, and R. Hadfield, "Superconducting nanowire single-photon detectors: physics and applications," *Superconductor Science and Technology*, vol. 25, 2012.
- [57] E. Herbst, "The chemistry of interstellar space," *Angewandte Chemie International Edition in English*, vol. 29, no. 6, pp. 595-608, 1990.
- [58] H. Daneshvar, et al., "Multilayer radiation shield for satellite electronic components protection," *Scientific Reports*, vol. 11, no. 1, pp. 1-12, 2021.
- [59] P. K. Samudrala, J. Ramos, and S. Katkooi, "Selective triple Modular redundancy based single-event upset tolerant synthesis for FPGAs," *IEEE Transactions on Nuclear Science*, vol. 51, no. 1, pp. 2957-2969, 2004.
- [60] R. Roche, et al., "A commercial 65nm CMOS technology for space applications: Heavy ion, proton and gamma test results and modeling," *2009 European Conference on Radiation and Its Effects on Components and Systems*, pp. 456-464, 2009.
- [61] A. Kerman, E. Dauler, and W. Keicher, "Kinetic-inductance-limited reset time of superconducting nanowire photon counters," *Applied Physics Letters*, vol. 88, no. 11, 2006.
- [62] K. Berggren, et al., "A superconducting nanowire can be modeled by using SPICE," *Superconductor Science and Technology*, vol. 31, no. 5, 2018.
- [63] T. Polakovic, et al., "Unconventional applications of superconducting nanowire single photon detectors," *Nanomaterials*, vol. 10, no. 6, 2020.
- [64] M. Castellani, "Design of Superconducting Nanowire-Based Neurons and Synapses for Power-Efficient Spiking Neural Networks," 2020.
- [65] B. Butters, "Digital and microwave superconducting electronics and experimental apparatus," 2022.
- [66] Q. Zhao, et al., "A compact superconducting nanowire memory element operated by nanowire cryotrons," *Superconductor Science and Technology*, vol. 31, 2018.
- [67] A. Maran, et al., "Use of the Seebeck effect for energy harvesting," *IEEE Latin America Transactions*, vol. 14, no. 9, pp. 4106-4114, 2016.
- [68] M. Grein, et al., "An optical receiver for the lunar laser communication demonstration based on photon-counting superconducting nanowires," *Advanced Photon Counting Techniques IX*, vol. 9492, 2015.
- [69] I Charaev, et al., "Single-photon detection in superconducting MgB2 micro-wires operating

up to 20 K,” 2021.

- [70] P. Caputo, et al., “High-performance magnetic field sensor based on superconducting quantum interference filters,” *Applied Physics Letters*, vol. 85, no. 8, 2004.